# From the Direct Observation of a PAA-Based Binder Using STEM-VEELS to the Ageing Mechanism of Silicon/Graphite Anode with High Areal Capacity Cycled in an FEC-Rich and EC-Free Electrolyte

Jianhan Xiong, Nicolas Dupré, Philippe Moreau, Bernard Lestriez

# From the direct observation of a PAA based binder using STEM-VEELS to the ageing mechanism of silicon/graphite anode with high areal capacity cycled in an FEC-rich and EC-free electrolyte

*Jianhan Xiong, Nicolas Dupré, Philippe Moreau, and Bernard Lestriez**

Jianhan Xiong, Dr. Nicolas Dupré, Prof. Philippe Moreau, Dr. Bernard Lestriez

Université de Nantes, CNRS, Institut des Matériaux Jean Rouxel, IMN, F-44000 Nantes, France

E-mail: bernard.lestriez@cnrs-imn.fr

**Keywords**: silicon/graphite anode, Polyacrylic binder, fluoroethylene carbonate, cell ageing mechanism, Li-ion batteries

**Abstract**. The polymer binder is a key constituent of silicon-based electrode formulation for lithium-ion batteries. However, its extremely difficult visualization in fresh electrodes becomes completely impossible in cycled electrodes. Here, the combination of STEM-VEELS with the use of a specific electrolyte solvent composition (a mixture of FEC and DMC, without EC) allows to visualize, for the first time, the binder in silicon-based even in electrodes cycled up to 100 cycles. Such an observation is possible thanks to the fact that the only solid degradation product of this electrolyte is LiF, as confirmed by quantitative $^{7}$Li and $^{19}$F MAS NMR. The binder (polyacrylic acid) is easily differentiable from LiF. The electrodes, based on a blend of silicon and graphite, have a very high surface capacity, 6.5 mAh / cm², i.e. 50% more than the state-of-the-art in graphite, which makes them meaningful for the EV

application. The performance are appreciable, in particular the first cycle efficiency approaching that of commercial graphite electrodes, as well as the capacity retention in full cell, vs. NMC532, 60 % after 100 cycles. This work also illustrates the ultimate state of destructuration of silicon after long cycling, which invites to think of new ways of designing this material.

## 1. Introduction

The drastic increase of Li-ion batteries (LIB) performance has been at the heart of the development of electric vehicles (EVs) for the past years. Increasing the autonomy of the latter requires improving the materials and design of the cells. Graphite, which is the negative electrode material used in commercial cells, has a moderate specific capacity and limits the charging rate of LiB due to the lithium-plating phenomenon that occurs at 0 V vs. $Li^+/Li$. The graphite-based electrodes have been optimized and no longer present a significant margin of progress.[1] The exploration of alternative negative electrode materials has recognized silicon (Si) as one of the most promising materials to significantly overtake graphite, thanks to its higher specific capacity (3579 mAh $g^{-1}$ vs. 372 mAh $g^{-1}$ for graphite). Other assets of this material are its low delithiation potential (0.4 V vs $Li^+/Li$), abundance and low cost. However, its use in commercial batteries still remains in practice very limited due to its strong cyclical variation in volume, which can reach 280 % in a completely lithiated state ($Li_{3.75}Si$). This results in an irreversible change in the morphology of the Si particles (fragmentation, nanoporosification) as well as severe mechanical damage to the electrode film (cracking, delamination of the current collector). In addition, the expansion / contraction cycles of silicon lead to a degradation of the solid electrolyte interphase (SEI), which must reform with each cycle.[2]

Many partial solutions have been proposed to increase the cyclability of negative silicon-based electrodes, such as the nanostructuring of silicon, the combination with carbon or other elements, in the form of composite or alloy, the mixture with graphite, designing the electrodes architecture, the use of electrolytic additives.[3–13] Numerous studies have underlined the key role of the binder on the cyclability of silicon-based electrodes. This one is essential for maintaining the cohesion of the electrode film and its adhesion to the current collector during cycling. The binder also acts more or less effectively as an artificial passivation layer.[14–16] The literature is abundant on this subject but it remains difficult to take advantage of it because few studies have been devoted to electrodes of loading and/or density high enough to be rationalizable for the application. A strong limitation in all studies relating to the binder is the difficulty of visualizing it. This one is in the form of nanometric deposits, on the surface or at the point of contact between the particles, which requires very high resolution techniques and/or sensitive to the presence of light elements.[17–20] Finally, the precipitation of the degradation products of the electrolyte masks the binder in all post-mortem studies. Although it is a key constituent of the formulation of silicon-based electrodes, the binder remains in most cases invisible to observation and its effects must be deduced from the more global measurements made on the electrode.

We are interested in this work in the electrochemical performance and the aging mechanisms in cycling of negative electrodes of very high capacity based on a mixture of silicon and graphite (mass ratio 1/1). These electrodes were formulated in water with the polyacrylic acid (PAA) binder for varying degrees of neutralization x in $PAAH_{1-x}Li_x$. This parameter is indeed crucial with respect to the electrodes manufacture quality and the interactions of $PAAH_{1-x}Li_x$ with the electrode materials and the electrolyte. A special feature of the present study is the use of an electrolyte highly concentrated in FEC, up to 30 %v, and free of ethylene carbonate

(EC).[21–23] Previous studies have highlighted the use of FEC as an important electrolytic additive to operate the Si/Gr electrode in the electrochemical cycle.[24–26] However, the FEC has only been added as an additive, usually at 10 % by weight.

A first work optimized and studied the role of the electrodes formulation on their initial properties and performance.[27] It has been shown that the electrodes prepared with the $PAAH_{0.85}Li_{0.15}$ binder, at an intermediate pH of 4, combine the positive assets of the electrodes prepared at more acidic and neutral pH, which lead to the best initial performance with a notable reversible capacity of 6.5 mAh $cm^{-2}$ and an initial coulombic efficiency of about 90%. These electrodes do not crack during the first cycles, unlike the other two, suggesting that the $PAAH_{0.85}Li_{0.15}$ binder has particularly favorable intrinsic mechanical properties, likely due to the moderate physical crosslinking of the binder by $Cu^{2+}$ ions originating from a slight corrosion of the copper current collector, and / or optimal interaction with the silicon surface. In a second study, sequential ex-situ FIB / SEM experiments showed the great resilience of the architecture of the electrode prepared with the $PAAH_{0.85}Li_{0.15}$ binder to the silicon volume variations.[28] Significant changes were only observed after ten cycles, due to a dramatic evolution of silicon particles which become nanoporous and therefore irreversibly increase in size.

Here, the mechanisms of chemical aging of these electrodes, prepared at different pHs (2.5, 4 and 6) and at iso-rheology (ensuring minimized homogeneity variations within the electrodes) are elucidated by combining scanning transmission electron microscopy (STEM) imaging, coupled with valence electron energy loss spectroscopy (VEELS), magnetic resonance characterizations nuclear magic angle (MAS NMR), and various electrochemical measurements. With the FEC-rich/EC-free electrolyte used in the present study, the only or major by far, electrolyte solid degradation lithiated product appears to be LiF. The absence of

other lithiated organic degradation products allows for the first time to visualize the PAA-based binder, its distribution at the surface of the active materials in the pristine electrode and its evolution throughout cycling. In addition, the electrochemical performance of these silicon/graphite electrodes, when combined with the $LiNi_{0.5}Mn_{0.3}Co_{0.2}O_2$ positive electrode, in full cells is remarkable, with around 60 % capacity retention after 100 cycles.

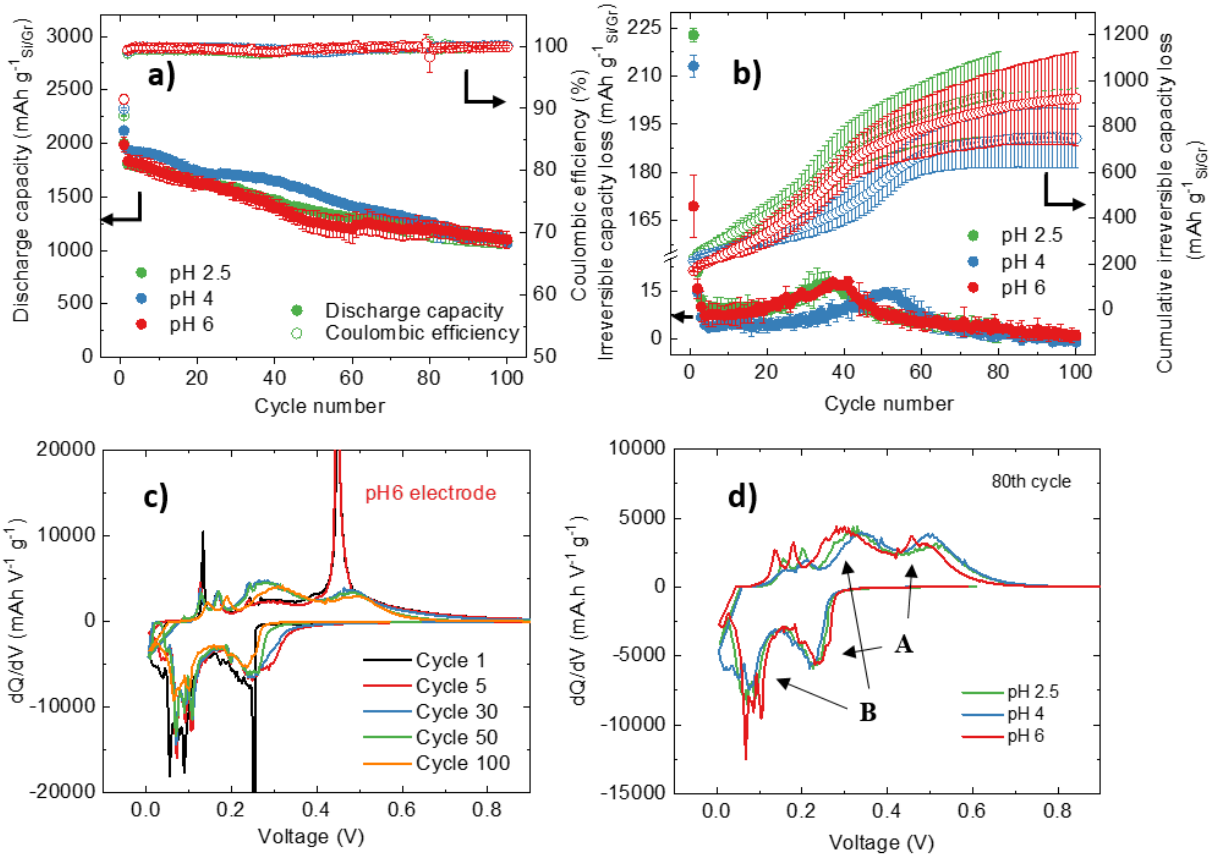


**Figure 1.** Half-cell electrochemical cycling of Si/Gr electrode prepared at pH 2.5, 4 and 6 (coin cells). a) Discharge capacity evolution; b) Irreversible and cumulative capacity loss vs. cycle number; c) Incremental capacity-voltage curve for pH 6 electrode during the electrochemical cycling, similar behaviors were observed for pH 2.5 and 4 at different cycles, except for 100$^{th}$ cycle; d) Comparison of incremental capacity-voltage curve for pH 2.5, 4 and 6 at 80$^{th}$ cycle.

## 2. Results

### 2.1. Si/Gr electrode ageing mechanism analyses

#### 2.1.1 Half-cell electrochemical cycling

Half-cell electrochemical cycling performance up to 100 cycles for electrodes based on PAAH (pH 2.5), $PAAH_{0.85}Li_{0.15}$ (pH 4) and $PAAH_{0.22}Li_{0.78}$ (pH 6) are given in **Figure 1a**. Corresponding voltage profiles and incremental capacity curves, which will be discussed later, are shown in **Figure S1** and **S2**. The highest initial reversible discharge capacity of 1920 mAh $g^{-1}$ is achieved for the electrode at pH 4, followed by 1820 mAh $g^{-1}$ for pH 6 and 1780 mAh $g^{-1}$ for pH 2.5. This superiority of pH 4 in terms of reversible discharge capacity is maintained up to 80 cycles. However, no significant difference could be noticed for all the pHs after 100 cycles. As a result, average discharge capacities of 1085, 1069 and 1102 mAh $g^{-1}$, corresponding to an areal capacity of 4.6 mAh $cm^{-2}$, are recorded at this stage for electrodes prepared at pH 2.5, 4 and 6, respectively. Some minor but interesting differences in their cycling behaviors can be noticed, which will be discussed later. The 1$^{st}$ cycle coulombic efficiency (CE) is equal to 88.8 %, 90.0 % and 91.5 % at pH 2.5, 4 and 6, respectively, and were discussed in our first study.[27] From the second cycle, the CEs are all above 99 %. The irreversible capacity loss at each cycle, $ICL_i$, is calculated as the specific capacity difference in lithiation and delithiation, named $Q_i^{\ lithiation}$ and $Q_i^{\ delithiation}$:

$$ICL_i\,(mAh\ g^{-1}) = Q_i^{lithiation} - Q_i^{delithiation} \qquad \text{(Eq. 1)}$$

The cumulative irreversible capacity loss is calculated as:

$$\text{Cumulative } ICL_i\,(mAh\ g^{-1}) = \sum_i (Q_i^{lithiation} - Q_i^{delithiation}) \qquad \text{(Eq. 2)}$$

Consistently with the CE values for the first cycle, the initial ICL appears to be the lowest for pH 6, at 170 mAh $g^{-1}$ (Figure 1b). Values at 213 and 223 mAh $g^{-1}$ are then found for pH 4 and 2.5, respectively. For each pH, an ICL peak is noticed, which translates into an abrupt increase of cumulative ICL between the $20^{th}$ and the $65^{th}$ cycles for the respective electrodes. This ICL peak is observed to reach its maximum between the $30^{th}$ and the $40^{th}$ cycle for the pH 2.5 and 6, but is clearly delayed to the $50^{th}$ - $60^{th}$ cycles for the pH 4. Similar evolution of the ICL along cycling was reported by Wetjen *et al.* for silicon/graphite blend electrodes, with a graphite to silicon ratio of 56:44.[29] The ICL peak was ascribed to an enhanced growth of the Solid Electrolyte Interphase (SEI) due to silicon particle morphological evolution, i.e. the transformation of dense particles to fluffy nanoporous ones, which results in a significant increase in their surface area and therefore in an increase in electrolyte degradation and in concomitant Li ions consumption. The decrease of the ICL after the peak maximum, was interpreted as an indication of attaining a steady-state silicon particle morphology exhibiting a lower rate of irreversible capacity; this steady state would result from the SEI cracking and electrolyte decomposition in response to repetitive volumetric changes. The ICL could also be due to a loss of Si/Gr electrochemical activity due to loss of electronic wiring of the particles as a consequence of their electrical insulation. The difference in the peak maximum location appears closely related to that of the observed capacity variation upon cycling (Figure 1a), as the electrode prepared at pH 4 shows a delay in the fading of its capacity compared to the two others. To understand this delay, one has to examine the two causes of degradation of these electrodes, (i) the chemical reason, linked to SEI accumulation and (ii) the mechanical reason, related to fracturing and interparticle contact losses.

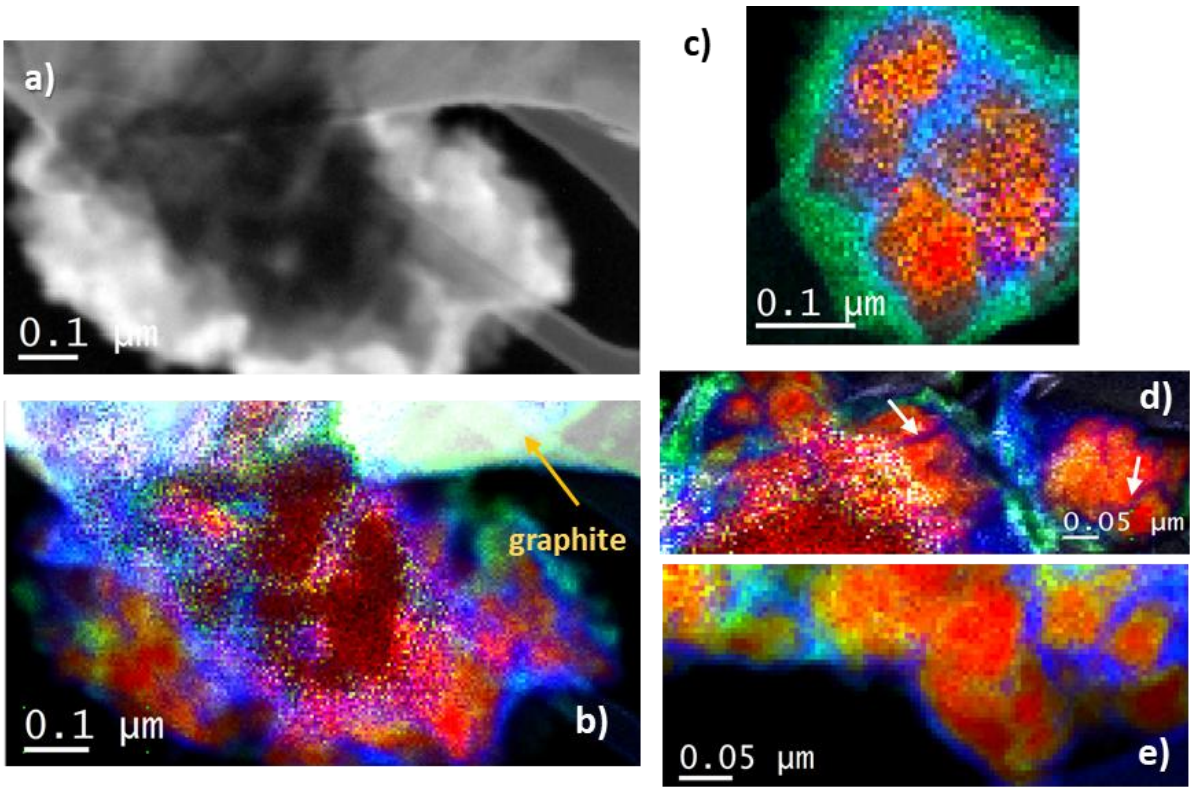


**Figure 2.** a) Typical STEM-HAADF image obtained on silicon electrode (pH 4 after 1 cycle) by selecting an energy plane (18.0-18.5 eV range) from the VEELS-SI data cube, which exacerbates the PAA-Li/LiF pixel intensities. b), c), d) and e) typical examples of quantitative maps after the 1$^{st}$ cycle b), d-e) on the pH 4 electrode and c) on the pH 2.5 one. Color code for the 4 phases: silicon (red), PAA-Li (blue), LiF (green) and graphite (light grey). The intensity of each color is linked to the absolute amount of the considered phase. The white arrows point the beginning of silicon pulverization and thus a new SEI occupation on the Si surface.

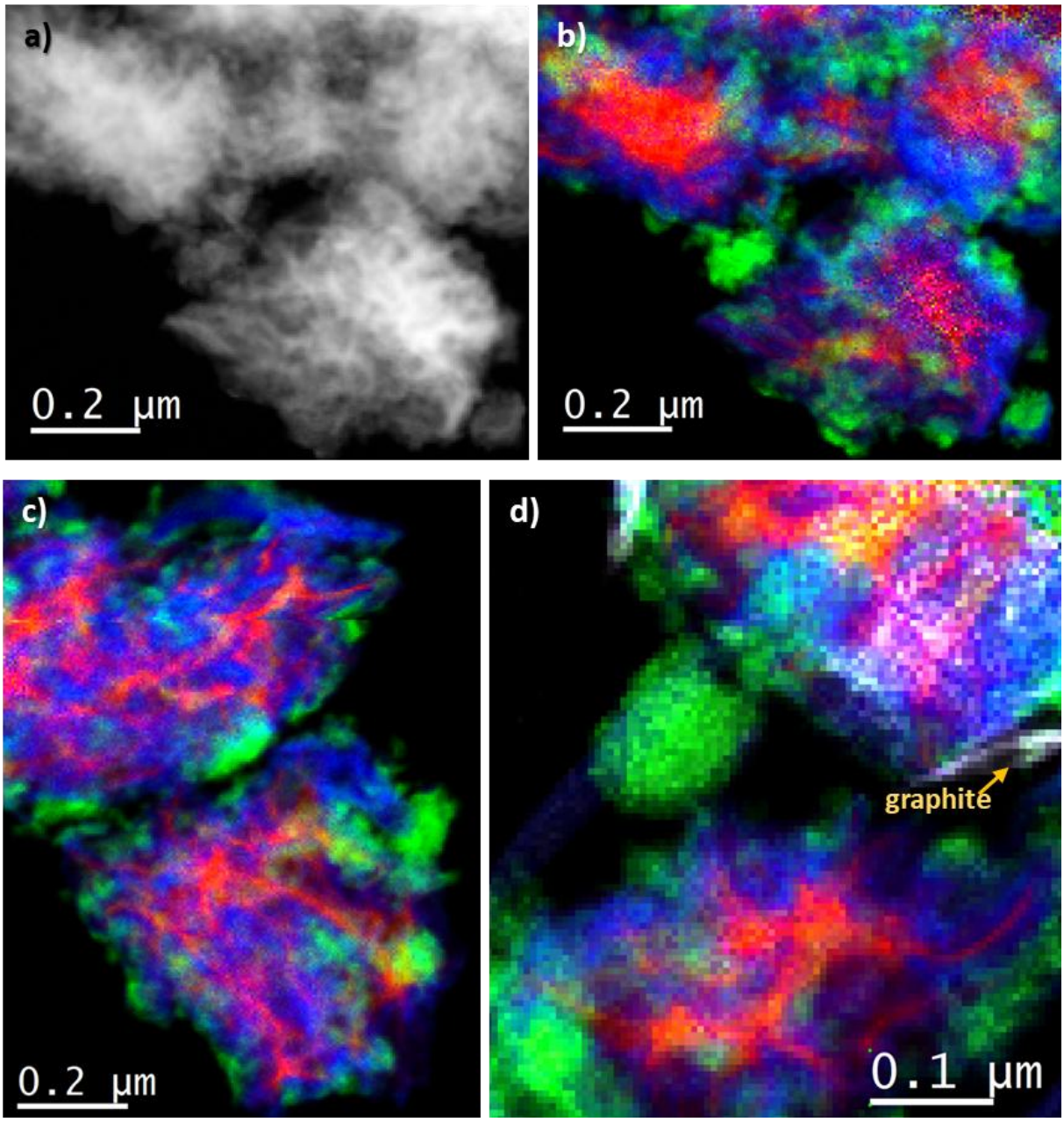


**Figure 3.** Example of a quantitative mapping on the cycle 30 pH 4 sample: a) STEM-HAADF image on silicon flakes; b) corresponding quantitative map of the repartition of the three phases (no graphite in this region). LiF clearly surrounds the polymer, itself surrounding the silicon filaments. c)-d) Other quantitative maps examples of the same electrode, the graphite (light grey) could be found in Figure d).

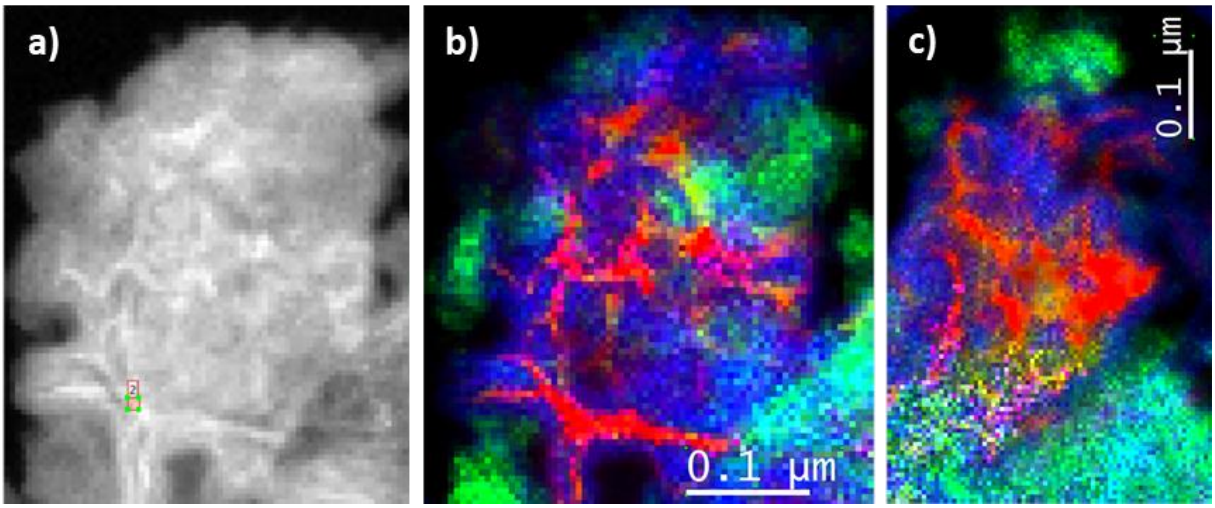


**Figure 4.** Example of a quantitative mapping on the cycle 100 pH 4 sample: a) STEM-HAADF image on silicon flake; b) corresponding quantitative map of the repartition of the three phases (no graphite in this region). c) Other quantitative map example of the same electrode. In both b) and c) the mixing of PAALi and LiF is visible at the bottom right where the turquoise color results from the blue (PAALi) and green (LiF) superposition.

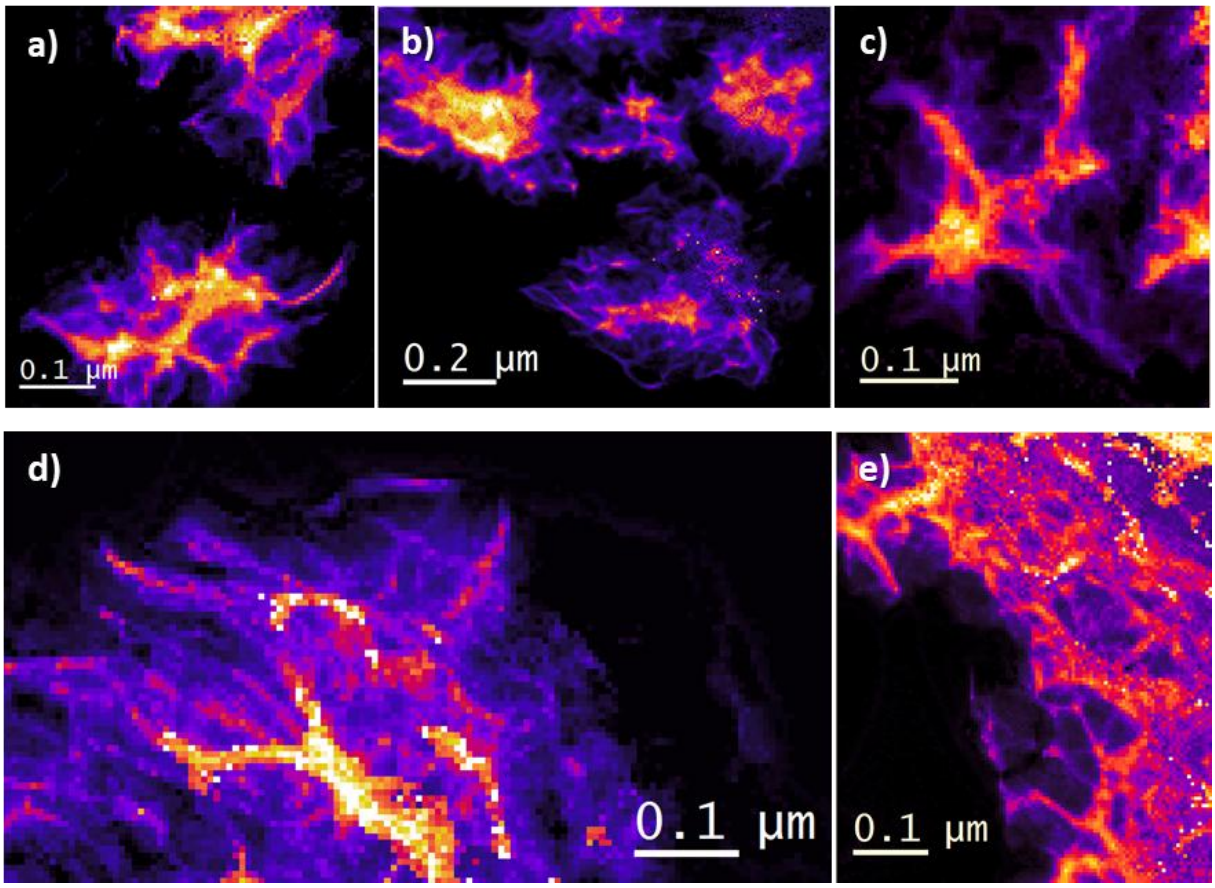


**Figure 5.** Examples of quantitative silicon phase maps for pH 4 and pH 6 samples a)-c) after 30 cycles and d)-e) after 100 cycles. Solely the silicon contribution is presented here. Instead of a linear red gradient used in all previous phase maps, the color scale was chosen as "black body extended" in order to better visualize the filaments and the "hairy" nature of the peripheral silicon around the cores.

### 2.1.2 STEM-VEELS studies

The STEM-VEELS observations were performed on Si/Gr electrodes prepared at pH 2.5, 4 and 6, after 1 and 30 cycles. For the pH 4 electrode, additional observations were also carried out in its pristine state after simple electrolyte immersion, and after 100 cycles. The morphological evolutions of the electrodes are studied through STEM-HAADF images and VEELS phase maps processed thanks to reference spectra (see experimental section and

supporting information **Figure S3** to **S6**). As a preamble, it should be noted that such observations can be only carried out on the clusters of the smallest particles for reasons intrinsic to measurement conditions. However, the initial particle size of the silicon powder used here is fairly widely distributed (from 0.2 to 3 µm).[28] It is known that the binder tends to concentrate in clusters of small particles during the last stage of solvent drying after electrode casting.[30] Consequently, the vision that is returned to us by these analyzes may not reflect all of the morphological and chemical changes that occur in these electrodes during their cycling.

The pH 4 electrode in pristine state and after simple electrolyte immersion was firstly studied (**Figure S7**). The silicon/graphite mixture appears intimate, signifying the particles of these two materials stick to each other, likely glued by the binder as evidenced by VEELS phase maps (**Figure S8**). Also, the silicon particles are noted dense. Negligible deposits of LiF on the active mass was observed after simple electrolyte immersion (**Figure S8**). The value of silicon plasmon is recorded at 16.72(2) eV with a full width at half maximum (FWHM) of 4.7(2) eV (**Figure S9**). The FWHM value, linked directly to the plasmon relaxation time, is significantly larger than that for crystalline silicon (3.7 eV[31]) and signifies a certain nanostructuring of the pristine particles. An example of such nanostructuring morphology could be found in Figure S9 and is typically obtained through a high-energy grinding.[32]

After 1 cycle, the silicon particles remain dense as in their original state (**Figure S10** and **S11**). The degree of intimacy of the Si/Gr mixture is preserved, whatever the pH (**Figure 2a,b)** of preparation of electrodes. Phase maps show that the binder (in blue) is present on and in-between the Si particles (in red), therefore ensuring their binding (**Figure 2c-e)**. For the pH 2.5 electrode, LiF (in green) appears forming an outer layer covering the binder (**Figure 2c**), while for electrodes prepared at pH 4 and pH 6, LiF forms distinct deposits that appear also

stuck on the binder layer (**Figure 2d** and **2e**). It should be noted that LiF seems to be the only degradation product detected, the only organic lithiated species being identified with PAALi, as explained in the TEM-VEELS analysis paragraph of the supporting information and as supported by MAS-NMR analyses. It is notable that the silicon sputtering has already started after 1 cycle (see white arrows in **Figure 2d**). The silicon plasmon has decreased slightly down to around 16.55-16.6 eV and the FWHM is slightly greater, around 5 eV (not shown), in agreement with a reaction/amorphization of the silicon.[33] The major difference between the different pH values after 1 cycle is therefore mainly the LiF location and distribution.

After the 30$^{th}$ cycle, a profound modification of the silicon morphology is observed whatever the pH of preparation of electrodes. Particles have all become nanoporous and flake-like shaped (**Figure 3a**). The position of the plasmon (Ep) is around 16.3-16.6 eV for silicon (not shown). This lower value compared to the one obtained for the first cycle could indicate a slight proportion of lithium trapped in the corresponding silicon areas.[33] This value is nevertheless very close to that of amorphous silicon and thus the lithium content is certainly lower than ~0.05 Li atom/silicon. The full width at half maximum of the plasmon peak is also much larger, 5-6 eV instead of 4.6 eV, in good agreement with the existence of a highly defective silicon. However, there is no major difference between the different pHs. Complementary STEM-HAADF images can be found in **Figure S12**. They notably show that the adhesion between silicon and graphite particles appears still maintained. Phase maps show the unambiguous presence of the binder around the silicon flakes, insuring mechanical bonding between them (**Figure 3b-d)**. However, compared to its morphology recorded after 1 cycle, the binder appears deformed, most probably in response of silicon repetitive distending. This indicates that the binder remains attached to the edge of silicon and therefore deforms with it, totally hugging its surface and thus still playing the role of artificial SEI. Furthermore,

it is noted that LiF forms deposits that are not systematically well bound to the binder shell around the silicon flakes, as shown in **Figure 3d**.

After 100 cycles, we constantly find the fluffy appearance of silicon with very few dense cores, as shown in **Figure 4a**. The energy of the silicon plasmon is systematically different from its initial value and is here recorded close to 14.4 eV, indicating a $Li_xSi$ alloy with x at approximately 1.5 ± 0.3. The corresponding FWHM is very high, more than 6-7 eV, which is also characteristic of $Li_xSi$ alloys. Interestingly, the composition is found homogeneous throughout the particle once the silicon morphology is completely fluffy, whereas for silicon particle made of a denser core surrounded by filaments, the lithium composition is lower in the filament-like parts than in the core. Such an example could be found in **Figure S13**. The binder is still found deformed around the branches/filaments of silicon. Both LiF deposits as well as mixture of the binder and LiF (turquoise color due to blue and green colors superposition in **Figure 4b and 4c**) are observed.

Phase maps representing solely the silicon contribution for electrodes cycled 30 and 100 times are given in **Figure 5**. They show the morphology of the fluffy silicon aggregates composed of nano-filaments, 5-20 nm in diameter. It can be noticed in **Figure 5a-c** that the filaments can be deployed to 100 nm long and they could also exist for the $Li_xSi$ alloys evidenced at the end of delithiation after 100 cycles as shown in **Figure 5d** and **5e**. The spatial resolution of the experiment (5 nm) is not enough to determine if indeed these filaments go through the expansion/shrinking sequence observed in typical micron-size silicon based electrodes. A number of statistics and adapted image processing would be necessary to quantify the silicon filament expansion, but the existence of lithiated filaments tends to indicate that they are still involved in the electrochemical process. The lower lithium content of the filaments compared to the core is also a good indication of this involvement (**Figure S14**), suggesting a better

reversibility of the electrochemical reaction in these thinner and more accessible parts of silicon particles. It is also interesting to notice that the distribution in space of the filaments defines structures with mesh size of the order of ~ 100 nm (**Figure 5e**), between cores or main filaments. Similar structures were also found in Boniface *et al.* after 100 cycles for a silicon material initially in the form of crystalline nanoparticles (70-150 nm diameter),[33] and also in the case of silicon nanowires.[34] We thus suggest that such filaments could be the ultimate structuration of silicon electrodes after prolonged cycling. Consequently, a pristine nano-structuration of silicon could help attaining the final steady morphology within a reduced time. In summary of the morphological and qualitative phase evolution, throughout the 100 cycles and whatever the pH of the slurry, the only electrolyte degradation product detected by TEM-EELS appears to be LiF (see also MAS NMR next section). This very original result could be linked to the specific composition of the electrolyte used here, rich in FEC and free in EC, which will be discussed later. The consequence of the formation of LiF only is that it has been possible to unambiguously visualize the polymeric binder in a cycled electrode, for the first time as far as we know. This one seems to continue to play its role of binder and of flexible artificial passivation layer throughout the cycling. Finally, the morphology of silicon particles changes drastically with the formation of a stringy and nanoporous structure, which could be the ultimate structuration of silicon after prolonged electrochemical cycling. This irreversible expansion of silicon must contribute significantly to the irreversible expansion of the electrode.

STEM-VEELS, through the knowledge of the local thickness, can also give supplementary information on a more quantitative way, with volume phase fractions in the sample deposited on the TEM grid. A detailed description of the process is described in the Supplementary Information part and results for pH 4 are gathered in **Table 1**. First of all, the volume fraction

of silicon appears to decrease progressively as a function of cycling, which is a result of the progressive pulverization of the electrode with aggregates leaving the main micron-size silicon particles (Figure S12). In order to follow the influence of the binder along cycling, we chose to concentrate our measurements on the external part of silicon particles, clearly more in contact with the PAALi binder after the electrode fabrication. We thus left unexplored "bulky micro-silicon" (Figure S12) containing a large proportion of the silicon. Such interpretation is also to be made for the percentage of graphite. Interested in the interaction of the PAALi binder with silicon and its effect on the SEI evolution, we disregarded graphite platelets, which are obviously still present after prolonged cycling (evidenced in Figure S12). The most interesting result is thus the quantification of the LiF evolution along cycling with respect to the PAALi binder close to it. The ratio LiF/PAALi increases dramatically from 0.07 (not cycled) to 0.41 (1 cycle), 0.50 (30 cycles) and 1.35 (100 cycles). Values for 1 cycle are already large if we consider that 29 cycles later, the ratio has increased moderately. The LiF production is thus occurring in large amounts right from the beginning of cycling and goes on steadily. A similar evolution of the LiF content will be presented in the next MAS NMR section. This evolution is markedly different from that observed with EC containing electrolytes where the constant production of organic/carbonates layers lead to a LiF/organic carbonates ratio around 0.2-0.3 even after 100 cycles.[35] It is worth mentioning that LiF/PAALi ratios after 30 cycles for pH 2.5 and pH 6 electrodes were measured to be 0.57 and 0.73, respectively. They are thus in the same order of magnitude with the pH 4 value. STEM-VEELS measurements do not identify a large difference reactivity at the SEI level as a function of the pH. Although performed on a large number of aggregates, this very local analysis (at a 5 nm scale) need to be confirmed and complemented with another technique

with larger sampling characteristics. MAS NMR spectroscopy results are thus presented in the next section.

**Table 1.** Volume percentages of phases obtained thanks to quantitative evaluation of STEM-VEELS maps at pH 4, as a function of number of cycles. In the case of 100 cycles, a composition $Li_xSi$ (x up to 1.5) is in fact often detected.

| | Not cycled | 1 cycle | 30 cycles | 100 cycles |
|---|---|---|---|---|
| vol% Si | 68 | 45 | 31 | 27 |
| vol% Graphite | 17 | 18 | 0 | 0 |
| vol% LiF | 1 | 11 | 23 | 42 |
| vol% PAALi | 14 | 27 | 46 | 31 |

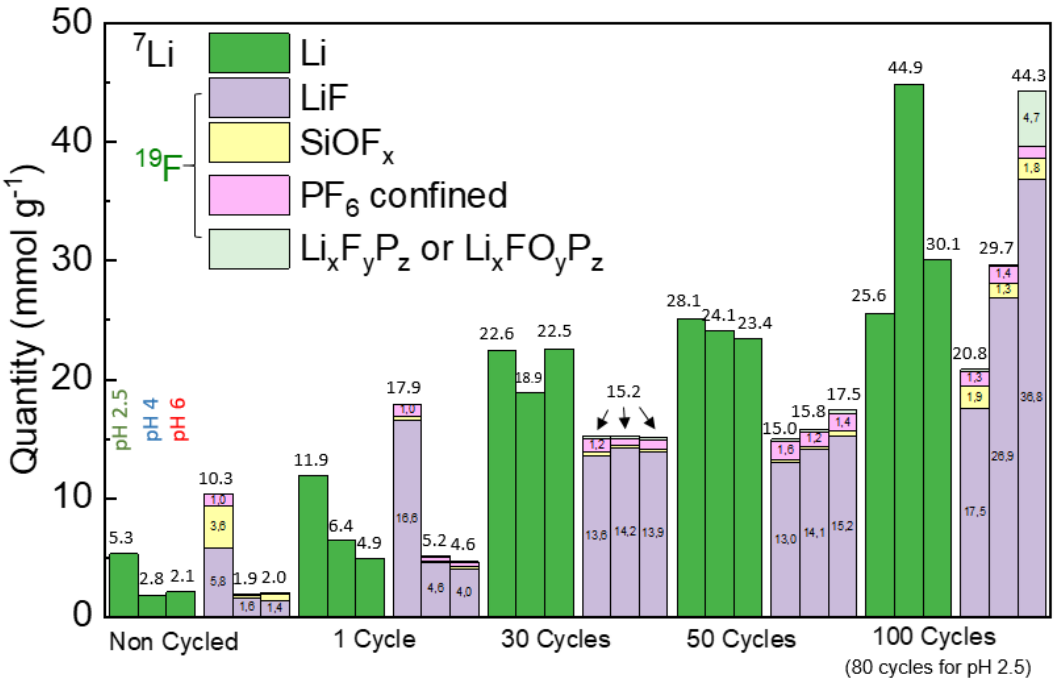

**Figure 6.** MAS NMR $^{7}$Li and $^{19}$F quantitative results of electrodes adjusted at pH 2.5, 4 and 6 non cycled and after the 1$^{st}$, 30$^{th}$, 50$^{th}$ and 80$^{th}$ (for pH 2.5) or 100$^{th}$ cycle.

### 2.1.3 MAS NMR spectroscopy.

The characterization of lithium and fluorine local environments, as well as their distribution at the surface of silicon and graphite active materials were carried out using $^{7}$Li and $^{19}$F MAS NMR. Representative *ex situ* samples were analyzed after exposure to the electrolyte prior to cycling and at the end of the 1$^{st}$, 30$^{th}$, 50$^{th}$ and 100$^{th}$ cycle for the electrodes prepared at pH 2.5, 4 and 6. MAS NMR experiments were intentionally performed at the end of delithiation in order to probe only Li nuclei present in the SEI, as it can be expected that all or most of the lithium was extracted from the silicon and graphite.[36–38] Therefore, the $^{7}$Li resonances corresponding to $Li_xSi$ environments should not be detected. This hold true for all samples measured according to STEM-VEELS results, except for the pH 4 electrode at 100 cycles as explained below.

$^{7}$Li and $^{19}$F NMR spectra and the attribution of respective chemical composition related to the local environments are presented in **Figure S15**. $^{7}$Li NMR peaks are observed with a maximum at -2 ppm and are assigned to the diamagnetic lithiated species deposited on the surface of active materials.[37,39] The asymmetry of the $^{7}$Li MAS NMR signal has been discussed in a previous study[27] and will not be discussed further here. Details are nevertheless given in supplementary information. The $^{19}$F NMR spectra of electrodes (**Figure S15b**) present four resonance peaks identified and considered for spectral fits. The major resonance visible at approx. -208 ppm, is assigned to LiF. A possible $SiO_xF_y$ contribution was detected at approx. -150 ppm, stemming from a reaction between the

electrolyte and silicon surface oxides.[40–42] The resonance identified at approx. -75 ppm was attributed to either residual $PF_6^-$ groups confined in SEI porosity remaining after the washing process. In some cases, a minor resonance peak could be detected at around -84 ppm also assigned to fluorophosphates such as $Li_xPF_z$ or $Li_xPO_yF_z$ species.[38]

The summary of $^7Li$ and $^{19}F$ quantifications of chemical species, deduced from the integrated intensities of $^7Li$ and $^{19}F$ MAS NMR spectra (**Figure S16a** and **S16b**, respectively), for electrodes prepared at pH 2.5, 4 and 6 prior to cycling and stopped at the end of charge after 1, 30, 50 and 100 cycles, are displayed in **Figure 6**. The results were obtained with the help of a calibration curve as described previously.[43] For the Li quantification, the number of moles of lithium used to neutralize the PAA in electrode slurry preparation was subtracted.

Results obtained prior to cycling and after 1 cycle, already discussed previously,[27] are reminded here for comparison purpose. It was concluded that, whatever the pH of preparation of the electrode, the lithiated species in the SEI correspond to almost only LiF and very little other species during the early stages of cycling in this EC-free and FEC-rich electrolyte. The electrode prepared at pH 2.5 exhibited the largest amount of electrolyte degradation products (LiF and $SiOF_x$) as a consequence of less efficient artificial SEI properties of the PAAH binder. Difference between the electrodes prepared at pH 4 and 6 were found to be minor. After the 30$^{th}$ cycle, both lithium and fluorine quantities clearly increased for all studied pHs. Amounts of lithium nuclei larger than for fluorine nuclei are detected. In the case of $^{19}F$ NMR spectra, due to extremely broad peaks, the background estimation and subtraction is challenging and may lead to a possible over-estimation of the amount of detected fluorine nuclei, suggesting the presence of lithiated species other than LiF. As seen in the previous section, TEM-VEELS characterizations indicated that the only lithiated electrolyte degradation product appears to be LiF while the lower values obtained for plasmon peaks

(16.3-16.6 eV after 30 cycles) point towards the presence of lithium trapped in silicon particles as $Li_xSi$ alloys. Then, we ascribe this additional amount of lithium, not combined with fluorine nuclei in LiF to the remaining lithiated silicon particles although the minor presence of other lithiated organic species stemming from the degradation of the electrolyte cannot be ruled out. The corresponding typical signals of Li local environments in $Li_xSi$ alloys could not be detected in the $^7$Li MAS NMR spectra. This particular feature is discussed and detailed in the paragraph below, in the light of the results obtained after 100 cycles.

Overall, upon cycling, respective amounts of lithium and fluorine become comparable whatever the pH of preparation of the electrodes. From the 30$^{th}$ to 50$^{th}$ cycle, the electrolyte degradation progressed very slowly. The SEI composition and distribution, as seen by $^7$Li and $^{19}$F MAS NMR does not show any significant differences between the 30$^{th}$ and the 50$^{th}$ cycles, whatever the pH of preparation. The absence of direct correlation between the continuous capacity fading observed for electrodes prepared at various pH and the variations in $^7$Li and $^{19}$F MAS NMR measured upon cycling clearly indicates that the capacity fading cannot be explained only by a continuous growth of a SEI containing electrolyte degradation products. It highlights the influence of other parameters such as electrode structure mechanical resiliency to the silicon volume variations. After the 100$^{th}$ cycle, results obtained for the electrode prepared at pH 2.5 has followed the same slow increasing trend toward a stabilization of lithiated and fluorinated species comprised in the SEI. One can note nevertheless an increase in LiF, from $^{19}$F estimation, while the amount of detected Li remains similar. In the case of the pH 6 electrode, an extremely broad peak is again obtained using $^{19}$F NMR, yielding an overestimation of the detected amount of LiF slightly larger than the total amount of lithium. It suggests nevertheless that almost all the lithiated species in the SEI correspond to LiF, in agreement with STEM-VEELS results. Furthermore, results obtained

for the electrode prepared at pH 4 differ significantly compared to the two previous cases. Firstly, a relatively larger amount of lithium is detected. The aspect itself of the $^{7}$Li MAS NMR spectrum is modified with an additional contribution centered at approx. 2 ppm (**Figure S16b**). While such a contribution is usually attributed to lithiated organic species coming from the degradation of the organic solvents,[36,41,44] previously discussed STEM-VEELS results indicate that no other lithiated species than LiF could be observed, in particular lithiated carbonates or semi-carbonates, while $Li_xSi$ alloys are clearly detected (**Figure S13 and S14**). The additional contribution observed in $^{7}$Li NMR at approx. 2 ppm is quite different from data that can be found in the literature where lithium poor alloys rise at 18 ppm and lithium rich alloys at approximately 6 ppm.[39] These shifts are observed in the case of the lithiation mechanism starting from crystallized silicon. In the present study, after tenths of cycles the silicon is fully amorphous and also nanostructured, which could lead to the detection of different $Li_xSi$ signals.[32,38] As a matter of fact, similar behavior has been observed for silicon nanowires consisting in a crystalline core with an amorphous shell.[34] In this case, it becomes quite difficult to distinguish surface Li (in the SEI) and Li in the $Li_xSi$ alloys due to strongly overlapping lines. It is also quite interesting to note that the morphological changes of the silicon after 100 cycles have led to the formation of 5 to 20 nm diameter nano-filaments (**Figure 5d-e**) and similar lithiation mechanism could occur in as-prepared nanowires and in the nano-filaments formed *in situ* in the present work. The formation of these nano-filaments was also observed after 30 cycles, consistent with the absence of detection of typical Li-poor (18 ppm) or Li-rich (6 ppm) $^{7}$Li MAS NMR resonances on the corresponding spectra. Overall, the amount of fluorine has also highly increased and the formed LiF gather approximatively two third of the total amount of lithium for the electrode initially prepared at pH4. It leaves a significant amount of lithium ions

trapped as $Li_xSi$ compared to the pH 2.5 and pH 6 cases. One possible and reasonable explanation may lie in the thick SEI and unfractured electrode as observed by SEM experiments (**Figure S17**) and detailed in the section below. It may be more difficult for Li ions to be extracted from the electrode prepared at pH 4, after 100 cycles, as the SEI deposits fill the porosity. In the case of electrodes prepared at pH 2.5 and 6, the cracks appearing across the electrode may in fact facilitate the electrolyte penetration into internal porosities, shortening the lithium extraction pathway. These results are consistent with results obtained in previous studies[45] in which the formation of micro-meter sized holes by laser drilling in Si/C composite electrodes significantly improves the performance due to the increased number of path available for lithium ion transfer to and from the active material. The obvious difference in our case is that the cracks are not under control. This is further discussed in the two sections below.

### 2.1.4 Macroscopic morphological evolutions

The SEM images corresponding to the surface of the electrodes are given in **Figure S17**. Wide views are presented here in order to display a visual overview of their overall mechanical integrity. Both pH 2.5 and 6 electrodes show a cracking after the first cycle, which is in contrast with the pH 4 electrode, for which very few cracks are observed, as confirmed with complementary FIB/SEM-interrupted experiments.[28] This difference in cracking in the first cycle were interpreted in our first work, on the basis of differences in physical crosslinking of the binder by copper (all the stronger as the pH of the slurry is more acidic), of differences in bonds between this binder and the surface of the silicon (more strong covalent bonds at acidic pH), and differences in the distribution of the binder at the surface of the active mass (homogeneous and thin coating layers for neutral pH vs. coarser deposits at

the more acidic pH). At the fifth cycle, the cracks were surprisingly erased from the surface of the electrodes. This is contrary to what has been observed for electrodes containing only silicon.[18,46] This could be due to the presence of graphite in significant content, which can promote laminar sliding within the electrode, as suggested by the FIB-SEM observations, due to its lubricating properties.[28] At the 30$^{th}$ and 100$^{th}$ cycle, cracks reappear on the surface of the electrode prepared at pH 6 and with a less extent at pH 2.5 (30$^{th}$ cycle). Complementary cycling with Swagelok cells performed under the same conditions (electrodes, loadings, electrolytes, current rate) as with coin cell, gives other evidences of significant variations in the mechanical behavior of the electrodes with the pH of preparation. Indeed, the lower internal pressure in the Swageloks causes greater expansion of the electrode film,[47] which is detectable in the electrochemical response and thus amplifies differences in electrodes mechanical properties (see **Figure S19** and its comments). As the amount of LiF precipitating in the electrodes is quite similar (**Figure 6**), we believe that these different mechanical behaviors during cycling could be attributed to a difference in the mechanical properties of the electrode with the preparation pH.

~~As seen by STEM-VEELS, the binder remains localized around the silicon particles and continues to establish links between them and with the graphite particles and therefore, is active in the role of maintaining the mechanical strength of the electrode. The electro-reduction of the carboxylic acid functions to lithium carboxylate during the first cycle should make interactions between the binder and the active materials surface relatively identical regardless of the pH of the electrode at the preparation. On the other hand, the copper-induced cross-linked binders (through copper carboxylate coordination bonds) could be at the origin of the better durability of the cohesion of the electrodes prepared at acidic pH with less cracking. Indeed, previous work has shown that the deliberate addition of cations (copper, etc.)~~

~~substantially improves the cyclability of silicon electrodes.[48] The much larger extent of copper collector corrosion at pH 2.5 maybe at the origin of an excessive crosslinking of the binder and lower ability to deform and maintain the electrode cohesion compared to the electrode prepared at pH 4~~. Additional particle size scale images at the scale of the particles can be found in **Figure S18** and show the accumulation of LiF deposits at the surface of the electrode.

### 2.1.5 Analysis of incremental capacity

In **Figure 1c-d**, plots of the incremental capacity evolution profiles at selected cycles for the pH 6 electrode (**Figure 1c**) and the comparison (**Figure 1d**) for the 80$^{th}$ cycle for the three electrodes are displayed. Noticeable difference with neutralization degree appears after the 50$^{th}$ cycle (**Figure S2**) and then amplifies with cycling, which is illustrated in **Figure 1d**. Interpretation of the incremental capacity evolutions between the 1$^{st}$ and the 5$^{th}$ cycles is in agreement with previous works and thus are described in Supporting Information.[32,49] In the following cycles, the electroactivity of silicon is characterized by two broad peaks (**Figure 1c-d**), A and B, ascribed to Li reactions with amorphous Si.[32,50] $Li_xSi$ alloys formed in step B are lithium-rich compared to those in step A. More precisely, in delithiation peak B can be attributed to the compositional equilibrium (biphasic process) $Li_{15}Si_4/Li_2Si$ and peak A to the transformation of the $Li_2Si/Si$ (via a solid solution). Lithium is however firstly extracted from graphite at 0.13 V, 0.17 V and 0.24 V. From the 5$^{th}$ cycle to the 50$^{th}$ cycle, a decrease of about 50 mV of the onset potential of Si lithiation is seen, marking an increase in the polarization of the cell (**Figure 1c**), reasonably due to an increase in the interfacial resistance of the electrodes, in agreement with the strong increase of interphasial species, as detected by MAS-NMR for all three pHs. Comparatively, the onset potential of peak B, upon lithiation of

silicon and those of the characteristic peaks of graphite in the same potential range appear to be less impacted, which is likely due to the stronger cell pressure at higher lithiation state (due to larger swelling of the lithiated silicon particles),[47] which minimizes contact resistances. At the 80th cycle, the electrode at pH 6 stands out very clearly with a much lower polarization in delithiation (**Figure 1d**). This observation does not correlate well with the amount of detected resistive LiF (**Figure 6**) and suggests that the reason for this higher polarization in the case of the pH 2.5 and pH 4 electrodes is not due to interfacial hampering but is rather due to diffusion limitations. Indeed, the presence of more numerous cracks in the electrode prepared at pH 6 (see SEM at 100$^{th}$ cycle in **Figure S17**) could make lithium diffusion easier through the electrode and could also impact the (de)insertion within the active materials. Indeed, in the case of the electrode prepared at pH 2.5 and 4, the lithium insertion and extraction must be done only via the tortuous porosity, while the presence of cracks at other pHs creates rectilinear and deep channels, not dissimilar to artificially laser-created micro-holes,[45,51,52] favoring rapid irrigation of these electrodes with electrolyte. …

The analysis of the electroactivity of silicon and graphite, that is to say the amount of respective phase still electrochemically active is now necessary to understand how the two active materials may be impacted by sluggish diffusion. Such an analysis is easier to perform on the delithiation curve, thanks to their better separated characteristic peaks.[49,53] Concerning graphite, we can see that the peak intensity at 0.13 V decreases by about half from the 1$^{st}$ to the 50$^{th}$ cycle for all pHs (**Fig. 1c** and **Figure S2**). This decrease is however more or less sudden according to the pHs. In comparison, from the 1$^{st}$ to the 30$^{th}$ or 50$^{th}$ cycle, the intensity of the peak at 0.17 V is invariant. This means that a fraction of the graphite particles might lithiate less deeply. From the 50$^{th}$ cycles, the graphite delithiation peaks shift to highest potential, in connection with an increase in the impedance of the electrodes. As mentioned

above, the polarization is less marked at pH 6 (**Figure 1d**). At the 80$^{th}$ cycle, the electrochemical activity of graphite is strongly decreased for the pH 4 electrode, which is attributable to the stronger polarization for this electrode in which the diffusion of lithium is more difficult due to the absence of cracks.

As for the analysis of the evolution of the electroactivity of silicon in delithiation, it is made more difficult by the increase in the intensity of the sharp peak at 0.45 V, from the 1$^{st}$ to the 5$^{th}$ cycle, then by its disappearance after the 5$^{th}$ cycle, which is then counterbalanced by the increase in peak B (**Figure 1c**). However, since about 90% of the total capacity of the electrode comes from silicon, it can be argued that the total capacity drop (**Figure 1a**) is attributable to a decrease in the amount of electroactive silicon. This is visible between 30$^{th}$ and 80$^{th}$ cycle, in particular on peak B. For the electrode prepared at pH 4, there is also a very strong increase in the polarization relative to the peaks B and A of silicon (**Figure 1d**), for the same reason as developed above (no cracks and sluggish lithium ions diffusion), indicating that the two active materials are equally impacted by the changes in the macrostructure of the electrode. Furthermore, at the 100$^{th}$ cycle, the lower peak B intensity for the electrode prepared at pH 4 compared to pH 6 (**Figure 2e**) appears in agreement with the trapping of lithium in the form of lithium-silicon alloys as detected by STEM-VEELS and MAS NMR.

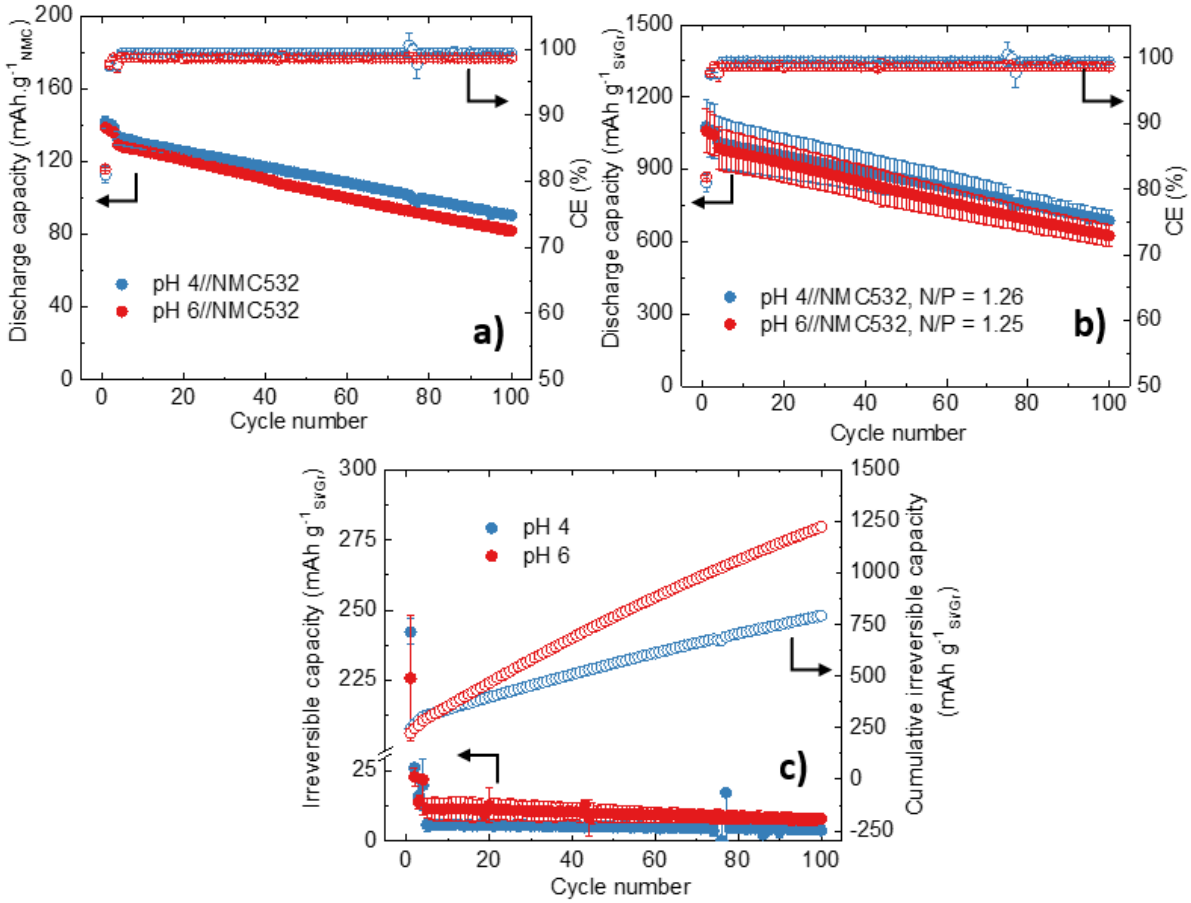


**Figure 7.** Full cell electrochemical cycling of Si/Gr negative electrodes prepared at pH 4 and 6 (coin cells) with NMC532 positive electrode. a) Discharge capacity in mAh per g of NMC vs. cycle number; b) Discharge capacity in mAh per g of Si/Gr vs. cycle number; c) Irreversible and cumulative capacity loss vs. cycle number.

**Table 2.** Parameters used in full cell test. The specific capacity considered for the NMC and Si/Gr electrodes is 151 and 1440 mAh $g^{-1}$ at C-rate of C/5, respectively, according to half-cell results. The N/P ratio was calculated considering the capacity of entire surface for NMC and Si/Gr electrodes.

| Electrode | Mass loading (mg $cm^{-2}$) | Diameter/surface ($mm/cm^2$) | Specific capacity (mAh $cm^{-2}$) | N/P ratio (mAh/ mAh) | Thickness (µm) | Porosity (%) |
|---|---|---|---|---|---|---|
| Si/Gr | 2.46 | 15/1.77 | 4.4 | 1.26 | 36 | 61.6 |

| | | | | | | |
|---|---|---|---|---|---|---|
| pH 4 | | | | | | |
| Si/Gr pH 6 | 2.45 | 15/1.77 | 4.4 | 1.25 | 36 | 62.9 |
| NMC | 26.0 | 12.7/1.27 | 3.9 | - | 76.6 | 23.6 |

**2.2. Si/Gr and NMC in full cell cycling**

Finally, the pH 4 and pH 6 electrodes were cycled in a full cell with a positive electrode based on NMC 532. The characteristics of the latter (composition, porosity, weight) are given in **Table S1**. Their cyclability in half-cells, facing metallic lithium, and with the same electrolyte as in this whole study, are given in **Figure S20**. Their cyclability was also studied with the standard LP30 electrolyte in **Figure S21**, showing inferior performance compared to the original composition used here (1 M $LiPF_6$ in DMC/ FEC 70/30 v/v). These results are in line with an increasing trend towards EC-free electrolytes in full cells.[54,55] **Table 2** gives the parameters of the full cells studied here.

The N/P capacity ratio is an important factor and was controlled at 1.25. The results (Discharge capacity, irreversible capacity or ICL and cumulative ICL) are shown in **Figure 7**. In **Figure 7a**, the evolution of the discharge capacity upon cycling is given in mAh per mg of NMC, as is usually shown. Along the 100 cycles, the cells show a regular and slow fading, contrarily to pure silicon-based electrodes for which abrupt capacity fade were previously observed in full cells at low number of cycles.[56] The capacity retentions remain close between the different pH of electrode. They are recorded at 60 ± 7 % and 59 ± 1 % for the electrodes prepared at pH 4 and 6, respectively. The cell using a pH 4 electrode shows slightly superior performance. The evolution of the discharge capacity upon cycling is given in mAh

per mg of Si/Gr in **Figure 7b**. Due to the higher capacity of the negative electrode than the positive one, silicon was not fully utilized. The comparison with the measurements in half-cells is therefore limited. The ICL and cumulative ICL are shown in **Figure 7c** and expressed in mAh per mg of Si/Gr. The ICL at the first cycle are equal to 242 ± 5 and 226 ± 22 mAh $g^{-1}$, at pH 4 and 6, respectively. These values match more or less the first cycle ICLs measured in half-cells (213 and 170 mAh $g^{-1}$, at pH 4 and 6, respectively). While the specific capacities measured after 100 cycles for the 2 electrodes are similar (**Figure 7a or b**), it is surprising to note that the corresponding cumulative ICL amounts to about 1220 mAh $g^{-1}$ for the pH 6 electrode, and only 790 mAh.$g^{-1}$ for the pH 4 one. This suggests a different behavior for the pH 4 electrode in terms of parasitic reactions and the corresponding amount of electrons measured by coulometry. In fact, the coulombic efficiency is slightly better for the pH4 electrode and could explain the divergent evolution of the cumulative irreversible capacity. Comparatively, the values were 921 and 748 mAh $g^{-1}$ for pH 6 and 4, respectively, in half-cells. It is important to note that the NMC electrodes do not display a stable cycling in half-cells. After 100 cycles the capacity faded to 128 mAh $g^{-1}$. In full cells, the capacity faded down to about 90 mAh $g^{-1}$. As the N/P ratio is superior to 1, the lithiation of silicon is incomplete. Therefore, all chemical and mechanical degradation of the silicon and graphite electrode is mitigated. As we could see in the characterizations relating to aging in half cells, the mechanical integrity of Si/Gr electrodes is fairly well preserved. The drop in capacity observed here in full cell configuration is then attributable to the loss of electrochemical activity of active materials subsequently to the loss of lithium inventory in the precipitation of the main degradation product of the electrolyte, namely LiF. The decrease in the electrochemical activity of the active materials also probably results from the irreversible morphological evolution of the silicon particles, which leads to a strong expansion of the

electrodes and probably to a decrease in efficiency of electronic percolation. This second mechanism is undoubtedly less significant in full cells here because silicon is not fully utilized and therefore less stressed, resulting in lesser morphological evolution. We can also note that the ICL is very regular in full cells, while in half cells the ICL has a maximum around 30-50 cycles which is linked to the deep morphological transformation of silicon. Thus, we can advance the main reason for the drop in capacity for these full cells is the trapping of the lithium initially provided by the positive electrode. Voltage profiles and incremental capacity plots are shown in **Figure S22**.

**3. Discussion**

The results obtained here call for discussion of previous work. There exist numerous electrolyte degradation products, which depends on the electrolyte composition and the surface chemistry of the active material.[15] The degradation of EC typically leads to the presence of $Li_2CO_3$ and polyethylene oxydes, $-(CH_2-CH_2-O)_n-$ (POEs). Parasitic reaction involving linear carbonates yield lithium alkoxides (ROLi) and lithium alkyl carbonates ($ROCO_2Li$). Traces of water, oxygen, silica, can give rise to $Li_2O$. LiF is found in the presence of fluorinated lithium salt and/or additives such as FEC. LiF can also be formed by attack of $Li_2O$ and $Li_2CO_3$ by HF. Fluorophosphates and phosphates are the decomposition products of the lithium salt $LiPF_6$. In the present case, the sole -or at least in very large majority- detected component of the SEI is LiF, which is surprising and deserves to be discussed in the light of the specific composition of the electrolyte used here, which does not contain EC and is rich in FEC (30 % by volume).

Different mechanisms for FEC reduction have been proposed. The products of its reduction differ according to the reaction mechanisms, to the composition of the FEC containing

electrolyte (FEC alone, FEC mixed with other solvents, presence or absence of lithium salt) and the presence and the characteristics of the electrode surface (in contact or not with silicon, use of a composite electrode or thin layer of silicon, crystalline or amorphous silicon, etc.). Nevertheless, studies are unanimous on the formation of LiF as a major constituent of SEI but disagree on the co-products of FEC reduction. Numerous studies conclude that a polymer is formed, generally crosslinked polycarbonate (polymeric fluorocarbonate or polymeric vinylene carbonate).[57–61] According to Schroder *et al.*, this conclusion could be biased by the presence of the polymer binder, in the case of composite electrodes, or even by brief exposure to air of the samples before their characterization.[62] Several works agree on the following reaction with 1 electron: FEC + $Li^+$ + $e^{*-}$ → LiF + $CO_2$ + $^*CH_2CHO$ where the last product is the vinyloxy radical.[21,60,61,63–65] In the electrolyte solution, this radical can then react with the various present solvents (FEC, EC, DMC, etc.) to yield numerous secondary products, the nature of which depend on the exact composition of the electrolyte. Recently, Jung et al., proposed a new reductive decomposition mechanism for FEC with the consummation of 4 electrons yielding $CO_2$, LiF, $Li_2O$, $Li_2CO_3$, $H_2$ and a partially cross-linked polymer.[25] However their electrolyte was a mixture of EC:EMC with up to 20 %wt FEC. $Li_2CO_3$ is a typical degradation product of EC.[37] Our results appears consistent with the reaction mechanism where the degradation products of FEC are LiF, $CO_2$, and the vinyloxy radical. Only LiF would be detected by the characterization techniques used here (STEM-EELS and MAS NMR). $CO_2$ is formed as a gas while products of the reaction of the vinyloxy radical with DMC (which is the co-solvent used here) or DEC are expected to be soluble in the electrolyte, preventing their detection with the characterization tools used in the present study. Our results would also suggest that the formation of $Li_2CO_3$ in non-negligible amount is favored when EC is used as co-solvent of the electrolyte. Such observation was in fact

previously made using the same STEM-VEELS technique,[33] where large amounts of lithiated carbonates were detected after prolonged cycling with a 1M $LiPF_6$ in EC:DEC (1:1) with 10 wt%FEC electrolyte.

Noteworthy, it is generally considered that the ionic conductivity of LiF is very low ($10^{-31}$ S $cm^{-1}$).[15] However, the atomistic molecular dynamics simulations of Jorn et al. indicate that a high concentration of LiF in contact with organic compounds, such as PAALi here, can allow for rapid transport of lithium ions, as the LiF ionic bonds can facilitate hopping-type transport mechanisms.[66] This consideration may help understanding why the Si/Gr electrodes studied here continue functioning after 100 cycles, even if a significant amount of LiF has precipitated on the surface of the PAALi/active mass. On the contrary, the behavior of Si electrodes cycled in an electrolyte containing EC with addition of FEC leads to the accumulation of EC-based degradation products (e.g. $Li_2CO_3$) that clog the porosity of the electrode, precipitating its end of life.[36,37] It is also generally believed that the strong internal cohesion of LiF increases the mechanical properties and the stability of SEI. The STEM-VEELS study highlights the critical role of the PAA polymeric binder as a pre-formed artificial SEI. It is reasonable to consider that its continuous covering of the Si surface along cycling helps in maintaining the LiF deposits attached to it (as seen in **Figures 3** and **4**).

Interestingly, the pH of the slurry or the degree of neutralization of the PAA has little influence on the capacity delivered after 100 cycles, even if behavioral differences are observed during cycling. Compared to many works about the polymer binder (see [27] and references therein), we have taken care to match the rheological properties of the slurries at different pH by adjusting the solid fraction. This makes it possible to minimize the variations in homogeneity in the composition of the electrodes, generally observed when the rheological properties are different, which can significantly influence the cyclability of the electrodes.

## 4. Conclusion

We have studied the ageing of high areal capacity 50:50 silicon/graphite negative electrodes upon electrochemical cycling. These electrodes were formulated with the $PAAH_{1-x}Li_x$ binder, their degree of neutralization varied from x = 0 to 0.78, corresponding to electrode slurries with pH varying from 2.5 to 6. A specific electrolyte composition, without EC, containing a mixture of DMC and FEC at 30:70 by volume and $LiPF_6$ salt was used to cycle these electrodes in half-cells against metallic lithium, and in full cells against NMC 532. The characterizations carried out by STEM-VEELS and MAS NMR show that the only or high majority solid degradation product of the electrolyte is LiF. It appears as deposits on the binder that forms an artificial passivation layer at the surface of the silicon and graphite particles. This pre-formed binder passivation layer probably limits the degradation of the electrolyte and maintains LiF deposits on the particles. In addition, it seems well adapted to cyclic volume variations of silicon, as well as to changes in the morphology of the silicon particles which become nanoporous and stringy during prolonged cycling. Despite these variations in volume and this irreversible change in morphology, causing in turn cyclic expansions and contractions of the electrode film, as well as an irreversible increase in its thickness, the cohesion of the electrode film is fairly well maintained at all of its scales and up to 100 cycles. The binder is expected to exhibit an identical molecular structure, after the electro-reduction of the carboxylic acid functions to lithium carboxylates at the end of the first cycle, for the three types of electrodes (prepared at pH 2.5, 4 and 6), whatever its initial degree of neutralization. However, the electrodes exhibit cycling differences which, while modest, are nonetheless noticeable, suggesting that there is a memory effect of their manufacture. Up to about 80 to 100 cycles, the electrode prepared at pH 4 shows the best

performance, with no cracking of the electrode film, less pronounced capacity fading, and a delay in the appearance of the irreversible capacity peak. This seems to be related to particular beneficial properties of the binder when mixed with other electrode components at pH 4. Its properties as artificial SEI, anchor for LiF deposits and the enhanced mechanical contacts maintenance between the particles are superior to those of the binders in the electrodes prepared at pH 2.5 and 6.

After a hundred cycles, the strongest cohesion of the electrode prepared at pH 4 turns against it, as illustrated by the more severe polarization measured for the pH 4 electrode. For electrode prepared at 6, macrocracks promote the penetration of the electrolyte and facilitate the diffusion of lithium within the thickness of the electrode film. The absence of such macrocracks forces the diffusion of lithium to follow the tortuous, LiF-filled porosity of the electrode. As a result, the delithiation of the electrode is clearly more difficult and incomplete, as supported by the unambiguous detection of $Li_xSi$ alloy using VEELS.

The cycling in full cells of these electrode formulations is quite satisfactory. Capacity retention is approximately 60% after 100 cycles. The electrode prepared at pH 4 shows modest but noticeable superiority to other electrodes. This invites to continue the efforts devoted to the search for new polymer binders based on coordination chemistry in order to modulate and optimize their mechanical properties and artificial SEI.

We attribute the superiority to the binder prepared at pH 4 to its physical crosslinking via the formation of copper carboxylate bonds, following a slight corrosion of the copper current collector during its coating with the acidic electrode slurry and subsequent drying. It requires further work for confirmation.

## 5. Experimental section

### 5.1. Materials

A blend of silicon and graphite (Si/Gr) was used as active material. The silicon powder used in the present study was obtained by milling a millimetric powder (99.96 % Si, 325 mesh, Materion), with a high-energy miller (Union Process attritor HD-01) taking a ball-to-powder mass ratio of 10:1 at 600 rmp for 20 hours under argon atmosphere.[32] The as-milled Si powder is nanostructured with micrometric agglomerates ($D_{v50}$ = 9.4 µm, $S_{BET}$ = 21 ± 1 $m^2$ $g^{-1}$). The electrochemical properties and performance of this silicon material in all-silicon electrodes have been studied elsewhere.[67–69] The graphite here is SFG6 from Timcal Timrex. GM15 (xGnP Graphene Nanoplatelets Grade M, thickness ~ 6-8 nm, $D_{avg}$ = 15 µm, XG Sciences) was used as a conductive additive. The selected binder was the polyacrylic acid (PAA) from Sigma-Aldrich (Mw ~ 450 kg $mol^{-1}$). It was used in non- or partially neutralized state, by adding LiOH.$H_2O$ salt (Sigma-Aldrich, white crystal), which will be specified in the results section. The water used was ultrapure (< 0.05 µS $cm^{-2}$).

### 5.2. Electrode preparation

The PAA binder is very hygroscopic and its use requires a pre-drying process for 3 h at 95 °C under vacuum to remove the adsorbed water. Before preparing the electrode slurries, the binder solution (PAA + (LiOH) + water) was stirred for at least 5 hours to reach the pH stabilization since the acid-base reaction PAAH + LiOH → PAALi + $H_2O$ is a slow process. The pH of PAA solution after the dissolution was stabilized at 2.5, or 4, or 6 depending on the amount of LiOH added, corresponding to a neutralization degree x of 0, 0.15 and 0.78 in $PAAH_{1-x}Li_x$. The electrode slurries were obtained by adding a total solid content of 400 mg comprising Si, Gr and GM15 to a PAA (or partially neutralized PAA) pre-dissolved solution. The slurries are then milled through a Fritsch Pulverisette 7 mixer with 3 silicon nitride balls (9.5 mm diameter) at 500 rpm for 1 h. Due to the viscosity increase with the pH of the

polymer solution, the rheological behavior of electrode slurry was adjusted with additional deionized water to maintain a similar electrode coating quality for all the pHs. The as-adjusted slurry was afterward tape cast onto a 25 µm thick copper foil (99.99%, MTI) at a blading speed of 5 mm/s. The electrode film was firstly dried at room temperature with limited airflow for one night before being punched out into disks of 10 mm diameter. A further drying step for 2 h at 120 °C under vacuum was done before battery assembly. The mass ratio of the electrode corresponds to Si/Gr/GM15/$PAAH_{1-x}Li_x$ 43:43:4:10. The Si/Gr loading varies between 3-3.5 mg $cm^{-2}$. Theoretical areal capacity of as-made electrodes is comprising between 5.9 - 6.9 mAh $cm^{-2}$.

**5.3. SEM imaging on the electrode surface**

To visualize the microstructure at the surface of the electrodes, SEM images were acquired using a high resolution scanning electron microscope JEOL JSM 7600F equipped with a field-emission gun operating at 2 kV. The cells are disassembled at the end of charge after the $1^{st}$, $5^{th}$, $30^{th}$ and $100^{th}$ cycle and washed by two drops of DMC and dried overnight under vacuum.

**5.4. Electrochemical measurements**

*5.4.1. Half-cell cycling*

Half cells were assembled in a glove box under argon atmosphere using CR 2032 coin cell configuration. The oxygen and moisture in glovebox were maintained lower than 0.2 ppm. The Si/Gr electrode was set as working electrode and a lithium metal foil (0.7 mm thick, Sigma-Aldrich) as reference and counter electrode. A borosilicate glass-fiber (Whatman GF/D) and a polyolefin based (Celgard 2500) discs were used as separators and were soaked with a 200 µL electrolyte consisting of 1 M $LiPF_6$ in dimethyl carbonate(DMC)/fluoroethylene carbonate (FEC) 70/30 v/v. The crimping pressure applied to the cell was 0.6 T. Electrodes were cycled with a VMP multichannel electrochemical potentiostat (Bio-Logic) in galvanostatic mode (GCPL) at a rate of C/16.5 during discharge

and C/8.2 during charge at 25 °C, corresponding to current densities of 120 mA $g^{-1}$ and 240 mA $g^{-1}$ respectively. The potential window was 0.005 – 1 V versus $Li^+$/Li allowing for a full capacity cycling. The specific capacity values are reported with respect to the total mass of active material Si and Gr. The acquired data were analyzed by EC-Lab software.

*5.4.2. Full-cell cycling*

Full cells were assembled under the same conditions as for half cells, except those specified in the following. $LiNi_{0.5}Mn_{0.3}Co_{0.2}O_2$ (NMC 532)-based positive electrodes were used to run the full-cell tests (see **Table S1**). Positive and negative electrodes were punched into discs of 15 and 12.7 mm respectively. The cells were cycled in GCPL mode, starting with three formation cycles at a rate of C/10 (referring to positive electrode in current case) for both charge and discharge process, and then at C/5 for the cycling. The potential window was 2.8 – 4.2 V between the Si/Gr and the NMC electrode.

**5.5. Magic Angle Spinning Nuclear Magnetic Resonance (MAS NMR) characterizations**

Electrodes collected from half-cell tests were stopped at the end of charge (delithiation) for MAS NMR analysis. They were collected from the disassembled CR 2032 cells inside the glovebox, rinsed with two drops of dimethyl carbonate (DMC) and dried under vacuum at 50°C for one night before being removed from the current collector. The resulting powder was then filled into a cylindrical 2.5 mm diameter zirconia rotor. $^7$Li and $^{19}$F MAS NMR measurements were carried out on a Bruker advance-500 spectrometer ($B_0$=11.8 T, Larmor Frequency $\nu_0(^7Li)$ = 194 MHz, $\nu_0(^{19}F)$ = 470 MHz). Spinning frequencies up to 25 kHz were used.$^7$Li NMR spectra were acquired with a single pulse sequence and a recycle time of 40 s. $^{19}$F NMR spectra were acquired using a Hahn echo sequence to discard the significant contribution from the probe signal and a recycle time of 30 s. Long recycle times were used to ensure quantitative measurements. All the spectra were normalized taking into account the number of scans, the receiver gain and the mass of the sample. $^7$Li and $^{19}$F integrated

intensities were determined by using spectral simulation Dmfit software,[70] taking the spinning sidebands into account. The absolute quantification of detected species was performed using i) a numerical fit and integration of each set of peaks corresponding to a chemical species, ii) a calibration curve obtained from reference LiF-Si or -Si/Gr mixtures.[43]

**5.6. Scanning transmission electron microscopy (STEM) – Valence electron energy-loss spectroscopy (VEELS)**

Scanning transmission electron microscopy (STEM) experiments were carried out using the Nant'Themis, a (S)TEM Themis Z G3 Cs-probe corrected microscope (Thermo Fisher Scientific) operated at 300 kV and equipped with a high-angle annular dark field (HAADF) detector. Electron energy loss spectra (EELS) were acquired by using a high resolution Gatan Imaging Filter 969, i.e. fitted with a CCD camera and a direct detection camera (K2), which was used in this study. Even if the Nant'Themis can be used with a monochromated beam, spectra were acquired with a 1.1 eV zero-loss peak (ZLP) width since it is sufficient for precise measurements of plasmon peak positions. A high energy dispersion (0.025 eV/pixel) was however used in order to spread the intensity over the 4000 pixels of high sensitivity K2 detector. Phase maps were acquired in spectrum imaging (SI) using the low energy loss part (valence) of the electron energy-loss spectrum (VEELS). Experimental conditions were very close to those developed by Boniface *et al.* and applied successfully on silicon electrodes.[33] In order to avoid electron beam damages a small convergence angle was used (4 mrad), a very low beam current (1 pA) and limited pixel time (40 ms). The electron dose is estimated to be 300 $e^{-}.Å^{-2}$, which is in the order of the maximum admissible dose previously determined.[35] Pixel sizes were also fixed to 5 nm to avoid beam damage overlap, value which approximately defines the spatial resolution of the maps. Even if the 300 kV acceleration voltage was higher than the optimal 200 kV, no beam damage could be evidenced.[35]

Processing of the VEELS-SI data cubes were performed in a similar way than that used by Boniface *et al.* but were all carried out within the DigitalMicrograph® (DM) software from Gatan.[71] Data cubes were realigned (ZLP), denoised (keeping 30 components), energy binned to get a 0.1 eV/pixel dispersion and Fourier-Log deconvolved. Silicon plasmon peak positions were fitted with a Drude-Lorentz[31] to a better than 0.05 eV precision. Similar results were obtained by fitting the energy maximum (less sensitive to the sometimes very large width of the plasmon region).[35] Each spectrum was then fitted with chosen components thanks to the MLLS routine in DM. Components were: graphite, LiF and Si spectra extracted from VEELS-SI of pure composition regions within our samples. A carbon based (without Li) spectrum from Boniface *et al.* was also tested and discussed in Supplementary section.[35] Finally, a PAALi spectrum obtained from a separated experiment performed on a pure PAALi sample was also included in the components. All reference spectra are given in the Supplementary section (**Figure S3** to **S6**). The percentages of phases in each pixel were given by the MLLS fit and quantitative maps (volumetric quantities) were produced thanks to the local thickness knowledge extracted from the calculated relative thickness map. Errors on the given values in each maps can be estimated to 5% taking into account fit, thickness calculation, statistic on pixel intensity calculation, etc. Due to the necessary selection of aggregates present on the TEM grid, weights of each phase in each VEELS-SI map of a same TEM grid can vary significantly. For example, Silicon phase volumetric quantity within two maps of the same TEM grid can vary from 10 et 30%. However, average values were proven to represent very reasonably SEI composition evolutions as well as its repartition within the aggregates.[35] Maps here presented are a representative selection of the results.

All electrodes were prepared in an Argon filled glove box, dried after cycling if cycled, scratched and deposited onto a lacey carbon film supported by a copper grid. The deposition

was obtained by simple contact of the powder with the lacey carbon film in order to avoid SEI modification in a DMC solvent, for example. A vacuum transfer sample holder (GATAN 648) was used to prevent any air contact of the reactive sample before its introduction into the Nant'Themis.

**Supporting Information**

Supporting Information is available from the Wiley Online Library or from the author.

**Acknowledgements**

We are grateful to the ANR for the funding of the SILMARILION project (ANR-16-CE05-0015) and to M. Chakir, L. Croguennec, C. Tessier, M. Ulldemolins, and B. Mortemard de Boisse for the fruitful discussions. N. Stephant is warmly thanked for the SEM images acquisitions. Also, funding by the French Contrat Plan État-Région and the European Regional Development Fund of Pays de la Loire, the CIMEN Electron Microscopy Center in Nantes, is greatly acknowledged.

Received: ((will be filled in by the editorial staff))

Revised: ((will be filled in by the editorial staff))

Published online: ((will be filled in by the editorial staff))

**References**

[1] M. Armand, P. Axmann, D. Bresser, M. Copley, K. Edström, C. Ekberg, D. Guyomard, B. Lestriez, P. Novák, M. Petranikova, W. Porcher, S. Trabesinger, M. Wohlfahrt-Mehrens, H. Zhang, *Journal of Power Sources* **2020**, *479*, 228708.

[2] M. N. Obrovac, V. L. Chevrier, *Chem. Rev.* **2014**, *114*, 11444.

[3] W.-F. Ren, Y. Zhou, J.-T. Li, L. Huang, S.-G. Sun, *Current Opinion in Electrochemistry* **2019**, *18*, 46.

[4] F. Dou, L. Shi, G. Chen, D. Zhang, *Electrochem. Energ. Rev.* **2019**, *2*, 149.

[5] Y. Zhang, N. Du, D. Yang, *Nanoscale* **2019**, *11*, 19086.

[6] Z. Liu, Q. Yu, Y. Zhao, R. He, M. Xu, S. Feng, S. Li, L. Zhou, L. Mai, *Chem. Soc. Rev.* **2019**, *48*, 285.

[7] J. Wu, Y. Cao, H. Zhao, J. Mao, Z. Guo, *Carbon Energy* **2019**, *1*, 57.

[8] S. Chae, S. Choi, N. Kim, J. Sung, J. Cho, *Angew. Chem. Int. Ed.* **2020**, *59*, 110.

[9] F. Li, J. Xu, Z. Hou, M. Li, R. Yang, *ChemNanoMat* **2020**, *6*, 720.

[10] J. Guo, D. Dong, J. Wang, D. Liu, X. Yu, Y. Zheng, Z. Wen, W. Lei, Y. Deng, J. Wang, G. Hong, H. Shao, *Adv. Funct. Mater.* **2021**, *31*, 2102546.

[11] M. Ge, C. Cao, G. M. Biesold, C. D. Sewell, S. Hao, J. Huang, W. Zhang, Y. Lai, Z. Lin, *Adv. Mater.* **2021**, *33*, 2004577.

[12] G. G. Eshetu, H. Zhang, X. Judez, H. Adenusi, M. Armand, S. Passerini, E. Figgemeier, *Nat Commun* **2021**, *12*, 5459.

[13] P. Li, H. Kim, S.-T. Myung, Y.-K. Sun, *Energy Storage Materials* **2020**, DOI 10.1016/j.ensm.2020.11.028.

[14] Y. Ma, J. Ma, G. Cui, *Energy Storage Materials* **2019**, *20*, 146.

[15] G. G. Eshetu, E. Figgemeier, *ChemSusChem* **2019**, *12*, 2515.

[16] S. Li, Y.-M. Liu, Y.-C. Zhang, Y. Song, G.-K. Wang, Y.-X. Liu, Z.-G. Wu, B.-H. Zhong, Y.-J. Zhong, X.-D. Guo, *Journal of Power Sources* **2021**, *485*, 229331.

[17] W. Porcher, S. Chazelle, A. Boulineau, N. Mariage, J. P. Alper, T. Van Rompaey, J.-S. Bridel, C. Haon, *J. Electrochem. Soc.* **2017**, *164*, A3633.

[18] C. R. Hernandez, A. Etiemble, T. Douillard, D. Mazouzi, Z. Karkar, E. Maire, D. Guyomard, B. Lestriez, L. Roué, *Adv. Energy Mater.* **2018**, *8*, 1701787.

[19] S. Müller, P. Pietsch, B.-E. Brandt, P. Baade, V. De Andrade, F. De Carlo, V. Wood, *Nat Commun* **2018**, *9*, 2340.

[20] K. L. Browning, R. L. Sacci, M. Doucet, J. F. Browning, J. R. Kim, G. M. Veith, *ACS Applied Materials & Interfaces* **2020**, 6.

[21] A. Schiele, B. Breitung, T. Hatsukade, B. B. Berkes, P. Hartmann, J. Janek, T. Brezesinski, *ACS Energy Lett.* **2017**, *2*, 2228.

[22] E. Zhao, Y. Gu, S. Fang, L. Yang, S. Hirano, *ACS Appl. Energy Mater.* **2021**, *4*, 2419.

[23] C. Erk, T. Brezesinski, H. Sommer, R. Schneider, J. Janek, *ACS Appl. Mater. Interfaces* **2013**, *5*, 7299.

[24] Z.-C. Wang, J. Xu, W.-H. Yao, Y.-W. Yao, Y. Yang, *ECS Transactions* **2012**, *41*, 29.

[25] R. Jung, M. Metzger, D. Haering, S. Solchenbach, C. Marino, N. Tsiouvaras, C. Stinner, H. A. Gasteiger, *J. Electrochem. Soc.* **2016**, *163*, A1705.

[26] C. C. Nguyen, B. L. Lucht, *J. Electrochem. Soc.* **2014**, *161*, A1933.

[27] J. Xiong, N. Dupré, D. Mazouzi, D. Guyomard, L. Roué, B. Lestriez, *ACS Appl. Mater. Interfaces* **2021**, *13*, 28304.

[28] V. Vanpeene, P. Soucy, J. Xiong, N. Dupre, B. Lestriez, L. Roué, *Journal of Power Sources* **2021**, 12.

[29] M. Wetjen, S. Solchenbach, D. Pritzl, J. Hou, V. Tileli, H. A. Gasteiger, *Journal of The Electrochemical Society* **2018**, *165*, A1503.

[30] S. Jaiser, J. Kumberg, J. Klaver, J. L. Urai, W. Schabel, J. Schmatz, P. Scharfer, *Journal of Power Sources* **2017**, *345*, 97.

[31] R. F. Egerton, *Electron Energy-Loss Spectroscopy in the Electron Microscope*, Springer US, Boston, MA, **2011**.

[32] M. Gauthier, D. Mazouzi, D. Reyter, B. Lestriez, P. Moreau, D. Guyomard, L. Roué, *Energy Environ. Sci.* **2013**, *6*, 2145.

[33] M. Boniface, L. Quazuguel, J. Danet, D. Guyomard, P. Moreau, P. Bayle-Guillemaud, *Nano Lett.* **2016**, *16*, 7381.

[34] L. Leveau, Etude de Nanofils de Silicium Comme Matériau d'électrode Négative de Batterie Lithium-Ion, Ph.D. thesis (French), Ecole polytechnique, **2015**.

[35] M. Boniface, Nanoscale Evolution of Silicon Electrodes for Li-Ion Batteries by Low-Loss STEM-EELS, Ph.D. thesis (English), University of Grenoble-Alpes, **2017**.

[36] Y. Oumellal, N. Delpuech, D. Mazouzi, N. Dupré, J. Gaubicher, P. Moreau, P. Soudan, B. Lestriez, D. Guyomard, *J. Mater. Chem.* **2011**, *21*, 6201.

[37] N. Delpuech, N. Dupré, D. Mazouzi, J. Gaubicher, P. Moreau, J. S. Bridel, D. Guyomard, B. Lestriez, *Electrochemistry Communications* **2013**, *33*, 72.

[38] N. Dupré, P. Moreau, E. De Vito, L. Quazuguel, M. Boniface, A. Bordes, C. Rudisch, P. Bayle-Guillemaud, D. Guyomard, *Chem. Mater.* **2016**, *28*, 2557.

[39] B. Key, R. Bhattacharyya, M. Morcrette, V. Seznéc, J.-M. Tarascon, C. P. Grey, *Journal of the American Chemical Society* **2009**, *131*, 9239.

[40] E. Lataste, C. Legein, M. Body, J.-Y. Buzaré, A. Tressaud, A. Demourgues, *J. Phys. Chem. C* **2009**, *113*, 18652.

[41] B. Philippe, K. Edstro, *Chem. Mater.* **2013**, 11.

[42] J. Bareño, I. A. Shkrob, J. A. Gilbert, M. Klett, D. P. Abraham, *J. Phys. Chem. C* **2017**, *121*, 20640.

[43] M. Cuisinier, J.-F. Martin, P. Moreau, T. Epicier, R. Kanno, D. Guyomard, N. Dupré, *Solid State Nuclear Magnetic Resonance* **2012**, *42*, 51.

[44] D. E. Arreaga-Salas, A. K. Sra, K. Roodenko, Y. J. Chabal, C. L. Hinkle, *J. Phys. Chem. C* **2012**, *116*, 9072.

[45] Y. Zheng, H. J. Seifert, H. Shi, Y. Zhang, C. Kübel, W. Pfleging, *Electrochimica Acta* **2019**, *317*, 502.

[46] V. Vanpeene, J. Villanova, A. King, B. Lestriez, E. Maire, L. Roué, *Adv. Energy Mater.* **2019**, *9*, 1803947.

[47] D. Vidal, C. Leys, B. Mathieu, N. Guillet, V. Vidal, D. Borschneck, P. Chaurand, S. Genies, E. De Vito, M. Tulodziecki, W. Porcher, *Journal of Power Sources* **2021**, *514*, 230552.

[48] D. Mazouzi, R. Grissa, M. Paris, Z. Karkar, L. Huet, D. Guyomard, L. Roué, T. Devic, B. Lestriez, *Electrochimica Acta* **2019**, *304*, 495.

[49] K. P. C. Yao, J. S. Okasinski, K. Kalaga, J. D. Almer, D. P. Abraham, *Adv. Energy Mater.* **2019**, *9*, 1803380.

[50] B. P. N. Nguyen, N. A. Kumar, J. Gaubicher, F. Duclairoir, T. Brousse, O. Crosnier, L. Dubois, G. Bidan, D. Guyomard, B. Lestriez, *Adv. Energy Mater.* **2013**, *3*, 1351.

[51] C. Xu, Q. Li, Q. Wang, X. Kou, H.-T. Fang, L. Yang, *Journal of Power Sources* **2021**, *492*, 229638.

[52] J. Park, C. Jeon, W. Kim, S.-J. Bong, S. Jeong, H.-J. Kim, *Journal of Power Sources* **2021**, *482*, 228948.

[53] S. Son, L. Cao, T. Yoon, A. Cresce, S. E. Hafner, J. Liu, M. Groner, K. Xu, C. Ban, *Adv. Sci.* **2019**, *6*, 1801007.

[54] S. Klein, S. van Wickeren, S. Röser, P. Bärmann, K. Borzutzki, B. Heidrich, M. Börner, M. Winter, T. Placke, J. Kasnatscheew, *Adv. Energy Mater.* **2021**, 2003738.

[55] L. Ma, S. L. Glazier, R. Petibon, J. Xia, J. M. Peters, Q. Liu, J. Allen, R. N. C. Doig, J. R. Dahn, *J. Electrochem. Soc.* **2017**, *164*, A5008.

[56] N. Delpuech, N. Dupre, P. Moreau, J.-S. Bridel, J. Gaubicher, B. Lestriez, D. Guyomard, *ChemSusChem* **2016**, *9*, 841.

[57] H. Nakai, T. Kubota, A. Kita, A. Kawashima, *Journal of The Electrochemical Society* **2011**, *158*, A798.

[58] V. Etacheri, O. Haik, Y. Goffer, G. A. Roberts, I. C. Stefan, R. Fasching, D. Aurbach, *Langmuir* **2012**, *28*, 965.

[59] E. Markevich, G. Salitra, D. Aurbach, *ACS Energy Lett.* **2017**, *2*, 1337.

[60] A. L. Michan, Bharathy. S. Parimalam, M. Leskes, R. N. Kerber, T. Yoon, C. P. Grey, B. L. Lucht, *Chem. Mater.* **2016**, *28*, 8149.

[61] I. A. Shkrob, J. F. Wishart, D. P. Abraham, *J. Phys. Chem. C* **2015**, *119*, 14954.

[62] K. Schroder, J. Alvarado, T. A. Yersak, J. Li, N. Dudney, L. J. Webb, Y. S. Meng, K. J. Stevenson, *Chem. Mater.* **2015**, 12.

[63] K. Leung, S. B. Rempe, M. E. Foster, Y. Ma, J. M. Martinez del la Hoz, N. Sai, P. B. Balbuena, *J. Electrochem. Soc.* **2014**, *161*, A213.

[64] J. M. Martinez de la Hoz, K. Leung, P. B. Balbuena, *ACS Appl. Mater. Interfaces* **2013**, *5*, 13457.

[65] M. Puget, V. Shcherbakov, S. Denisov, P. Moreau, J.-P. Dognon, M. Mostafavi, S. Le Caer, *Chem. Eur. J.* **2021**, chem.202100562.

[66] R. Jorn, R. Kumar, D. P. Abraham, G. A. Voth, *J. Phys. Chem. C* **2013**, *117*, 3747.

[67] D. Mazouzi, D. Reyter, M. Gauthier, P. Moreau, D. Guyomard, L. Roué, B. Lestriez, *Adv. Energy Mater.* **2014**, *4*, 1301718.

[68] S. Rousselot, M. Gauthier, D. Mazouzi, B. Lestriez, D. Guyomard, L. Roué, *Journal of Power Sources* **2012**, *202*, 262.

[69] Z. Karkar, D. Mazouzi, C. R. Hernandez, D. Guyomard, L. Roué, B. Lestriez, *Electrochimica Acta* **2016**, *215*, 276.

[70] "Home | dmfit - D.Massiot - NMR@CEMHTI CNRS UPR3079 Orléans France," can be found under https://nmr.cemhti.cnrs-orleans.fr/dmfit/default.aspx, **n.d.**

[71] "Gatan Microscopy Suite Software | Gatan, Inc.," can be found under https://www.gatan.com/products/tem-analysis/gatan-microscopy-suite-software, **n.d.**

[72] S.-J. Tambio, H. Roberge, J. Xiong, P. Soudan, N. Besnard, B. Lestriez, *J. Electrochem. Soc.* **2021**.

# Supporting Information

## From the direct observation of a PAA based binder using STEM-VEELS to the ageing mechanism of silicon/graphite anode with high areal capacity cycled in an FEC-rich and EC-free electrolyte

*Jianhan Xiong, Nicolas Dupré, Philippe Moreau, and Bernard Lestriez**

I – Potential profiles and incremental capacity curves of Si/Gr electrodes in half-cells (coin cells).

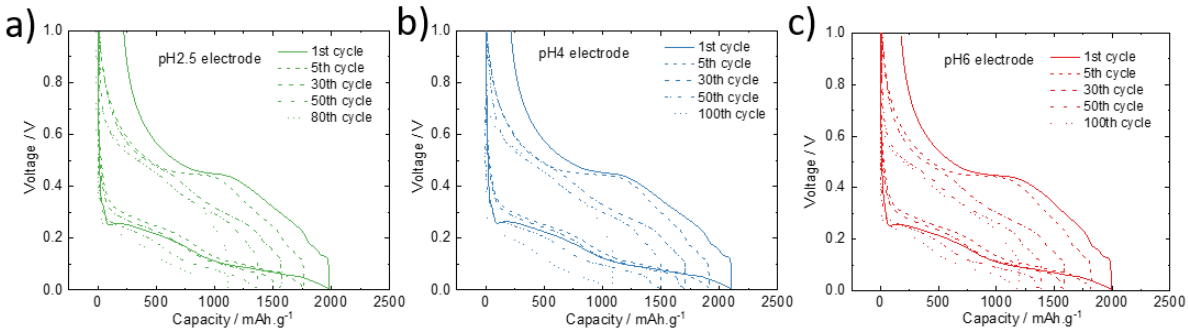


**Figure S1**. Voltage profile of the Si/Gr electrodes prepared at a) pH 2.5, b) pH 4 and c) pH 6 for the 1$^{st}$, 5$^{th}$, 30$^{th}$, 50$^{th}$, and 100$^{th}$ cycle.

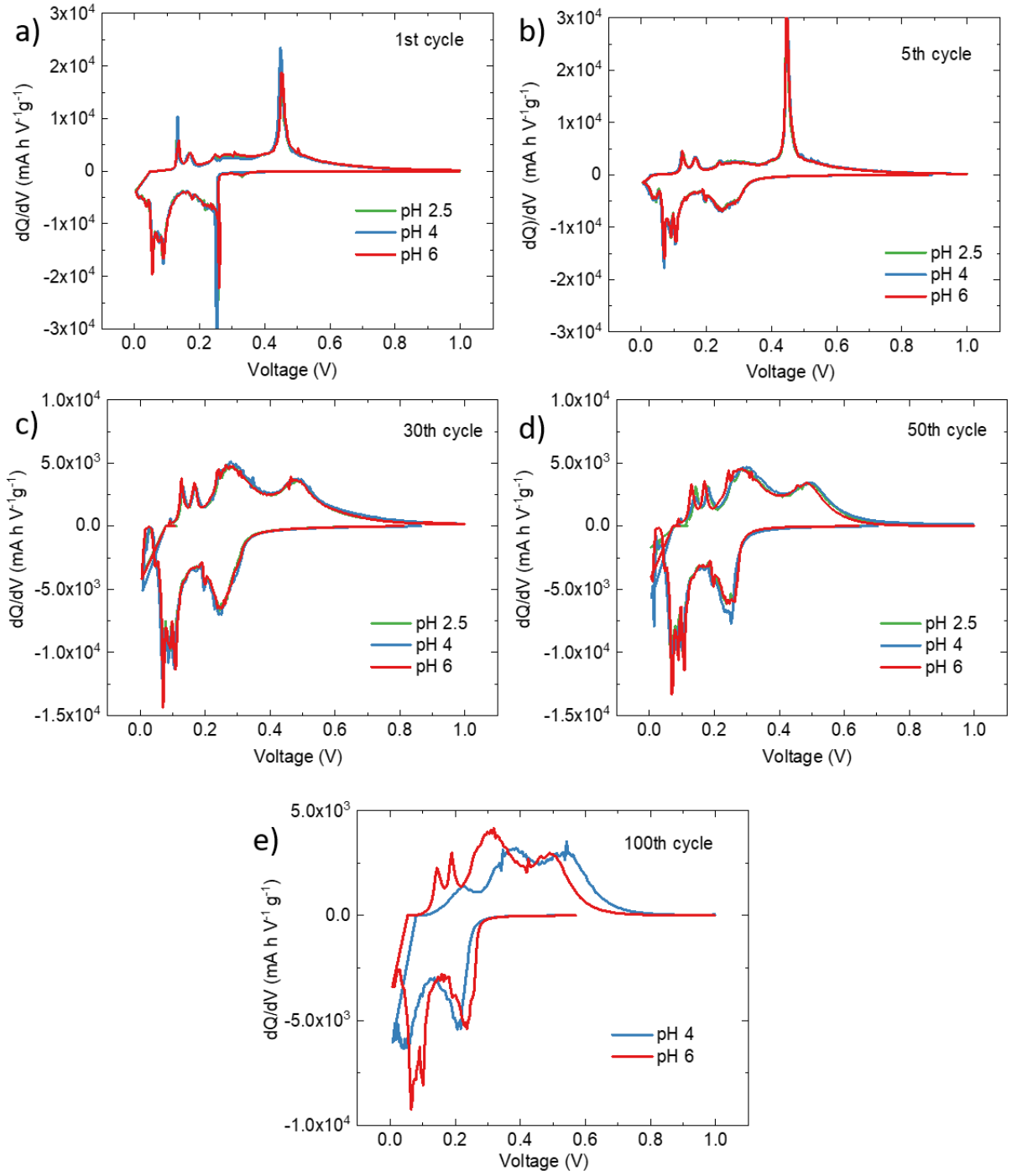


**Figure S2.** Comparison of incremental capacity curve of pH 2.5, 4, and 6 electrodes for the: a) 1st, b) 5th, c) 30th, d) 50th and e) 100th cycles.

During the first discharge (**Figure S2a**), individual contributions of silicon and graphite to the global electrochemical behavior are well defined, whatever the pH of preparation of the

electrodes. Incremental capacity peaks located at 0.26 V and 0.07 V reveal the electroactivity of silicon while graphite contributions are found at 0.18 V, 0.09 V and 0.06 V. The sharp peak at 0.26 V is related to the lithiation of partially crystallized pristine silicon powder. During the subsequent charging process, lithium is firstly extracted from graphite at 0.13 V, 0.17 V and 0.24 V. Lithium dealloying from silicon appears as a broad peak around 0.3 V followed by a sharp peak at 0.45 V. The latter is resulting from the transformation of the crystalline $Li_{15}Si_4$ compound into an amorphous $Li_2Si$ phase through a two-phase reaction. During the first cycle, the lithiation/delithiation mechanism of the silicon used here is typical of a mixed amorphous/crystalline silicon, which in the present case is ~30% crystalline.[27] Subsequent cycles, at least until the 5$^{th}$, suggest an easier lithiation of the silicon, as the first incremental capacity peak onsets at 0.4 V, which is mostly due to the amorphization of the silicon (**Figure S2b**). Simultaneously, the intensity of the sharp peak at 0.45 V in delithiation increases from the 1$^{st}$ to the 5$^{th}$ cycle. This peak is however only visible during the early stages of the electrochemical cycling (at least 5 cycles).

II - STEM-VEELS analysis

**Determination of the phases in the VEELS-SI maps. -** In order to identify phases in the VEELS-SI maps, components have to be chosen appropriately. In case of two very similar components, the MLLS fit might lead to some large errors on weights attributed to these two very similar phases. This is the case for the choice of the polymeric nature of the signal identified in the SEI: PAALi is an obvious choice of component but a polymer without Li could also be presumed, a priori. As an example, we show in the following the effect of the inclusion, or not, of this component “Organic no Li” (organic polymer without Lithium) in the MLLS fit, hence in the resulting maps. Such reference spectrum was obtained from a previous

study.[35] All reference spectra here discussed are presented in **Figure S1**. In **Figure S2a**, a representative VEELS-SI data cube is presented along with color maps of the different phases with (in b) and without (in c) the "Organic no Li" component. It is clear from the two color maps that the LiF, graphite and Si components are barely affected by the following discussion (compare green, white and red pixels). In order to pinpoint the fit issue on the polymeric part, three small regions (labelled 1, 2 and 3 in **Figure S2a**) were extracted and their decomposition in components given in **Figure S3** and **S4**.

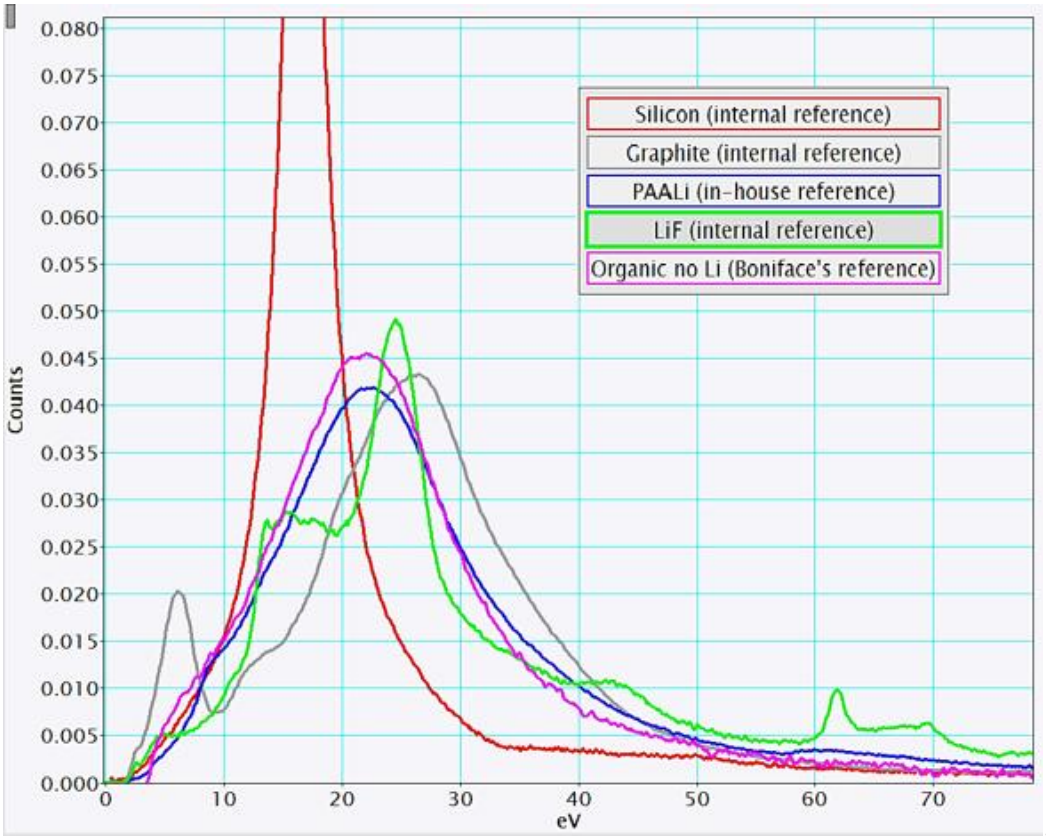


**Figure S3.** All reference spectra used in the MLLS process. Spectra for LiF, graphite, and Si were extracted from VEELS-SI obtained in this study ("internal references"). The PAALi spectrum was obtained from a separated experiment specifically performed (using the same experimental conditions) to obtain this reference spectrum ("in-house reference"). Note the similar shape of the PAALi (blue) spectrum and polymer marked "Organic no Li" (pink) spectrum.

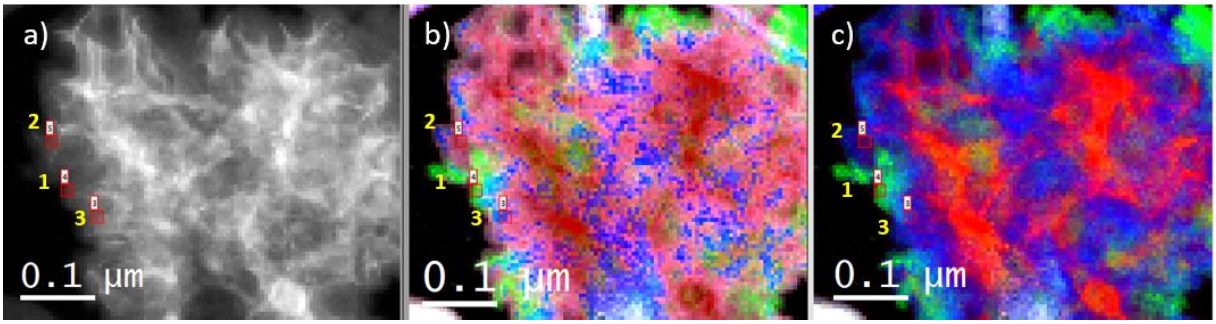


**Figure S4.** a) VEELS-SI obtained on a representative sample (pH 4 at 30$^{th}$ cycle). Energy plane around 16.8 eV, i. e. characteristic of Silicon. b) Color map of phases obtained after MLLS fit of the VEELS-SI in a). In this case, all components presented in Figure S1 were used. Notice the blue and pink intermixing. c) color map of phases obtained after MLLS fit of VEELS-SI in a). In this case, all components but the "Organic no Li" were used. Obviously, solely a PAALi (in blue) contribution is obtained. Color code: PAALi (blue), silicon (red), LiF (green), graphite (light grey), "Organic no Li" (pink).

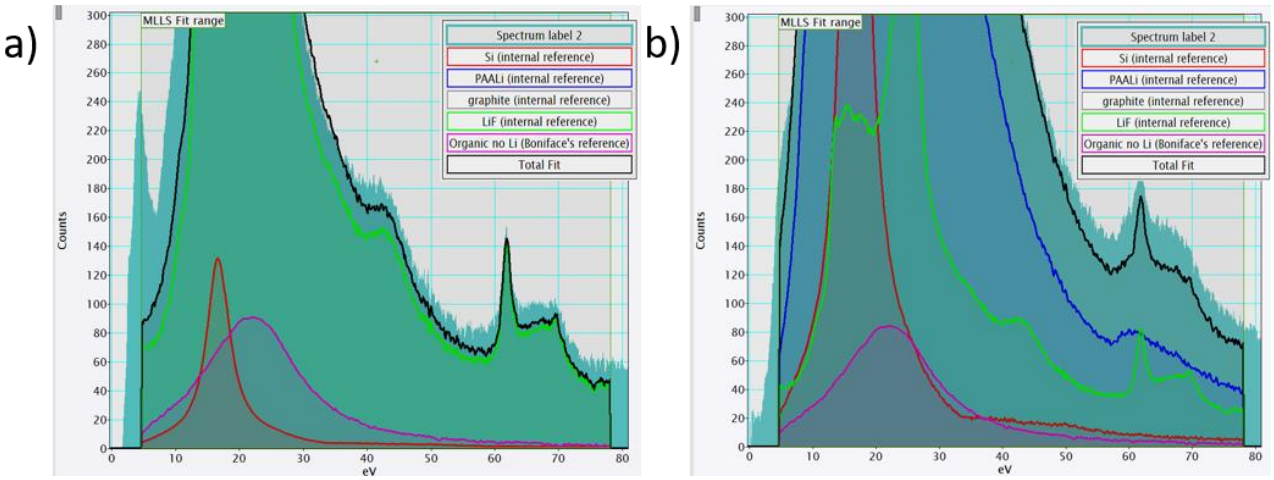


**Figure S5.** a) MLLS fit decomposition for the region labelled 1 in **Figure S5a**. The region is clearly identified as almost purely made of LiF. b) MLLS fit decomposition for the region labelled 3 in **Figure S4a**. The region appears to be identified as made of a large proportion of PAALi (and some LiF).

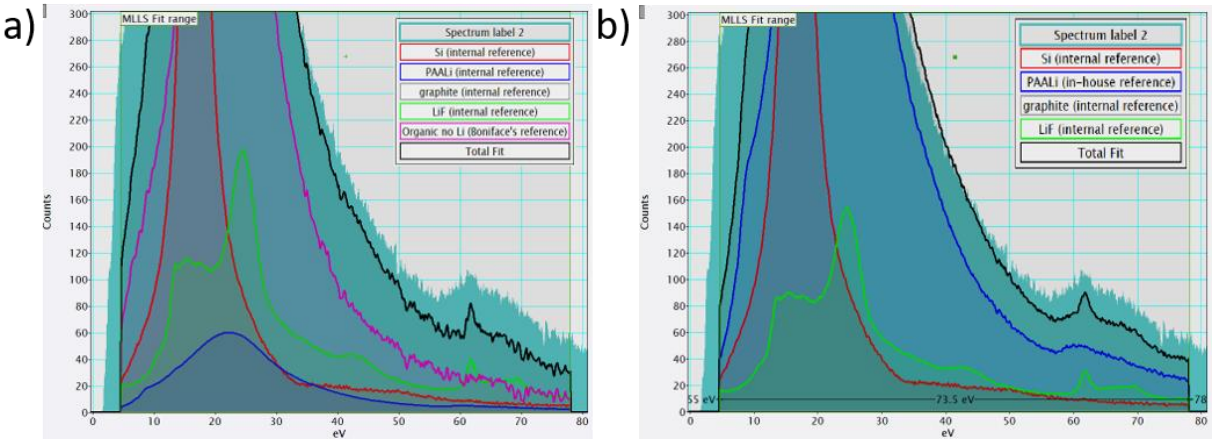


**Figure S6.** MLLS fit decompositions for the region labelled 2 in **Figure S4a**. a) Fit obtained with all the components, i. e. with "Organic no Li" spectrum. b) Fit obtained without the "Organic no Li" spectrum. All being equal, the fit appears actually better with a smaller number of components (without the "Organic no Li" spectrum).

In the case of region 1, the decomposition is very efficient and reliable in identifying LiF (**Figure S5a**). For region 3, the MLLS fit identifies properly a strong PAALi contribution (**Figure S5b**). The shape of the Li-K edge at around 60 eV is a clear mixture of the PAALi signal with that of the LiF. For region 2, probably because of the importance given to the spectrum in the 10-30 eV range, the fit is much worse around the Li K-edge. This leads to the attribution of a strong "Organic no Li" contribution (pink line, **Figure S6a**), which seems unjustified to the naked eye. If one performs the MLLS without this contribution, the fit appears actually better and is consistent with the presence of PAALi in this region as well (**Figure S6b**). Consequently, it seems unjustified to take into account a contribution of a polymer not containing lithium for quantification of phases in the VEELS-SI data cubes. It is impossible to rule out any presence of such contribution, but it is most probably a minority phase and would lead to erroneous weights for the phase quantification.

**STEM imaging of initial electrodes**. - The pH 4 electrodes in pristine state and after simple electrolyte immersion were studied. However, their analyses revealed to be difficult. As the cohesion strength within the electrode is strong, most of fragments have a size too large for

the TEM observation. In the present study, only a few small clusters could be examined. Under TEM examination, these two samples differ only slightly, thus solely images of the pH 4 electrode after electrolyte immersion are presented here in **Figure S7**.

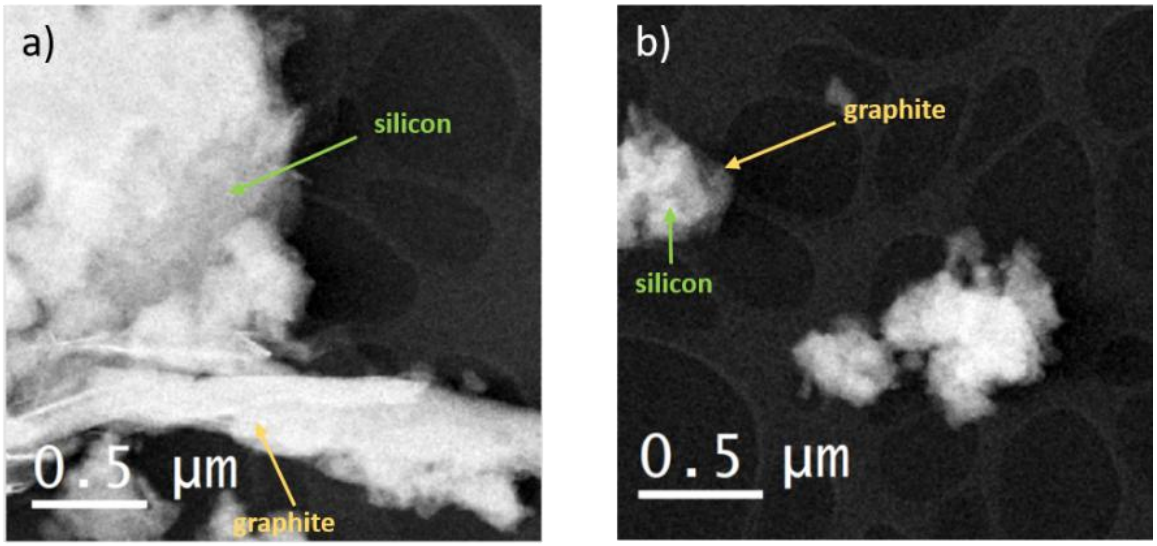


**Figure S7**. a) Typical STEM-HAADF images obtained on silicon electrode at pH 4 before cycling. Images can be noisy due to the low current used to avoid electron beam damages. Graphite flakes (seen here edge-on in bottom part) in close contact with a large silicon agglomerate (top left); b) Typical clusters analyzed by VEELS-SI. The top-left aggregate is actually a flat graphite flake with silicon a cluster on top.

**Negligible presence of LiF deposits before cycling. -** Samples analyzed by VEELS-SI are prepared by drying the electrodes. Since they have been in contact with the electrolyte containing $LiPF_6$, such a process could produce by itself some degradation products, such as LiF. In order to determine the extent of electrolyte degradation during the drying process, an electrode was immersed in the electrolyte (pH 4), was dried according to the same protocol as to cycled electrodes, and analyzed. Percentages of LiF phase were always minimal, of the order of a few percent (or less) in all VEELS-SI maps. Three typical examples are given in **Figure S8**. Most representative is the measured quantity of PAALi compared to that of LiF: the ratio PAALi/LiF is usually way above 10. At the same time, it can be seen that the PAALi

indeed surrounds the smallest aggregates and covers bigger particles in the form of a thin layer.

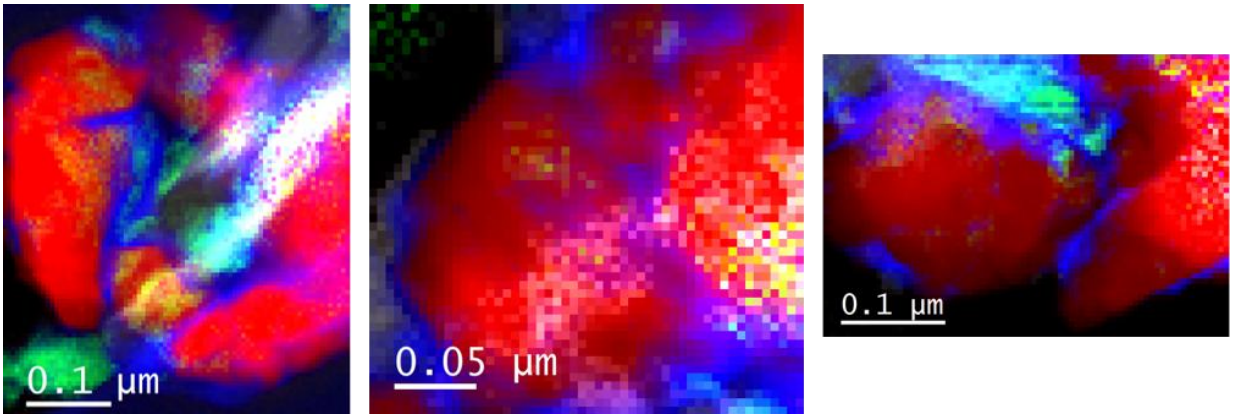


**Figure S8.** Quantitative phase maps obtained by MLLS of VEELS-SI data in the case of a pH 4 electrode just immersed in electrolyte. Color code: PAALi (blue), silicon (red), LiF (green), graphite (light grey). Note the PAALi is usually around smaller silicon particles and insures some binding between them and the graphite flakes (see left hand side map).

**Nanostructuration of pristine electrodes. -** In **Figure S9**, an example of such nanostructuring in the pristine silicon material (before cycling) is presented. The silicon aggregate presents a constant volume plasmon energy (**Figure S9a-b**), in agreement with its unaltered silicon nature (electron volumetric density is always the same). Conversely, the FWHM of this plasmon increases significantly in some areas from 4.6 to 5.1 (**Figure S9c**, green regions). These regions present a significantly lower relaxation time (inversely proportional to the width) and evidence regions with high concentration of defects. Nano-regions of ~ 50 nm are clearly seen (in blue) and prefigure the future pulverization occurring with electrode cycling.

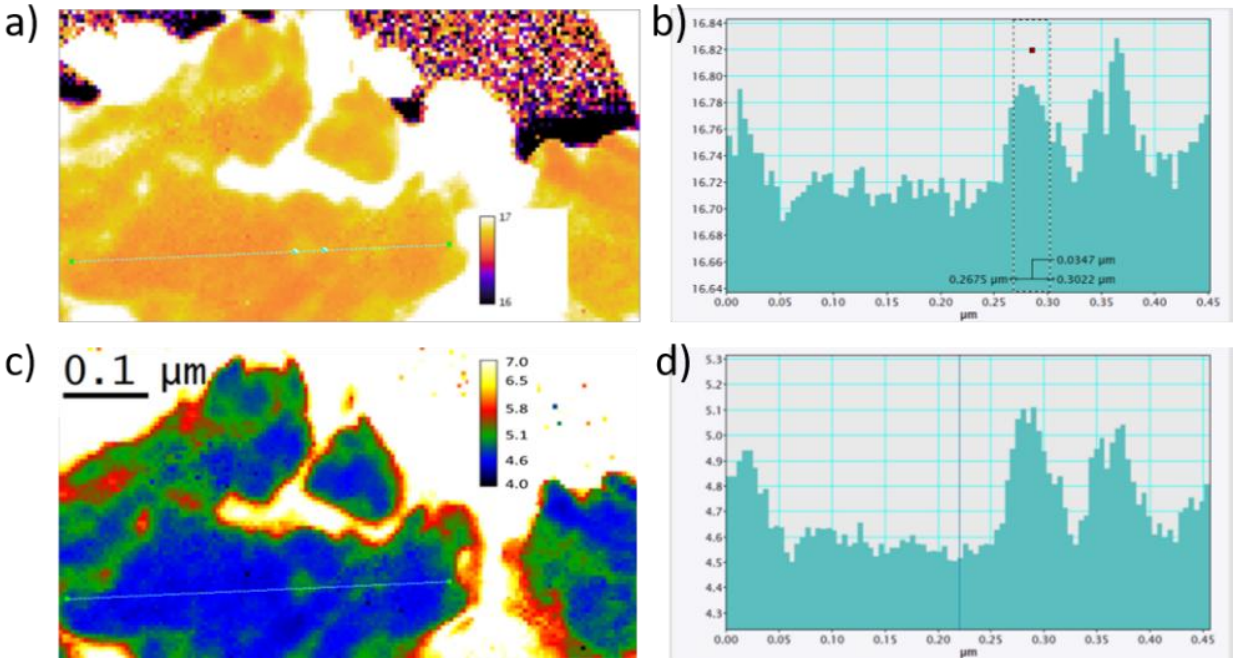


**Figure S9.** a) Map of plasmon energy values ($E_p$). Values at surface of aggregates and outside the aggregate are obviously irrelevant; b) Energy values corresponding to the trace in a), showing a typical 16.72(2) eV value; c) Map of plasmon FWHM (ΔEp) for the same region as in a); d) Trace along the line drawn in c) showing a typical 4.7(2) eV value.

**STEM-HAADF images of Si/Gr electrodes after 1 cycle.**

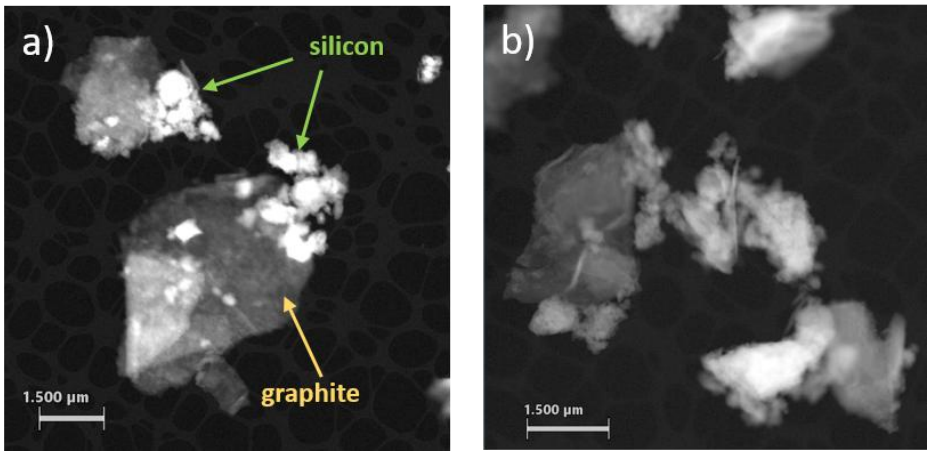


**Figure S10**. Typical STEM-HAADF images obtained on a silicon-graphite electrode (pH 6 after 1 cycle). The graphite flakes can be clearly identified. White areas are silicon particles/aggregates. Core of silicon aggregates are denser (thus appear whiter). Edges of such aggregates are usually less dense as a consequence of the beginning of their pulverization.

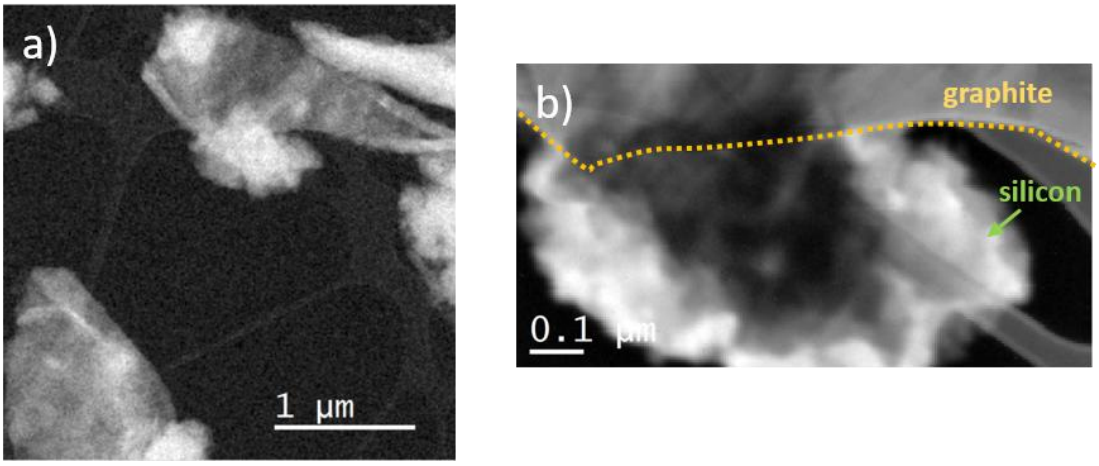


**Figure S11.** a) Typical STEM-HAADF image obtained on silicon electrode (pH 4 after 1 cycle). The graphite flakes can be clearly identified. White areas are silicon particles/aggregates; b) Part of image a) obtained by selecting an energy plane (18.0-18.5 eV range) from the VEELS-SI data cube. The graphite is seen here flat (at the top of image) and a silicon aggregate can be seen in contact with it. This plane exacerbates the PAA-Li/LiF pixel intensities (See also Figure 2a, b). The dark mass at the center of the image is a dense silicon particle that did not react, hence did not become fluffy.

**STEM-HAADF images of Si/Gr electrodes after 30 cycles.** - At pH 2.5 (**Figure S12a-b**), the graphite slabs can be clearly identified as straight pieces either lying flat or edge on. Regarding the TEM image (**Figure S12c**) of pH 4 electrode, the graphite slabs can be clearly identified around the middle of the image, seen partly edge-on. A piece of graphite is also seen embedded in the silicon de-structured aggregate (above the middle of the image). The **Figure S12d** demonstrates a good interaction between graphite and silicon at pH 4 even after 30 cycles. The graphite is seen here flat and some silicon aggregates can be recognized, whiter and filamentous on the top. The image is an energy plane (16.5-17.5 eV range) from the VEELS-SI data cube. This plane exacerbates the silicon pixel intensities where silicon signal is strong. The large silicon particles (> 5 microns) in **Figure S12e** seem to keep a less unstructured core. We could observe the white flakes shaped nanoporous silicon and graphite are located on top or around, as well as a bulky micro-silicon, which is highlighted by a green arrow on the image.

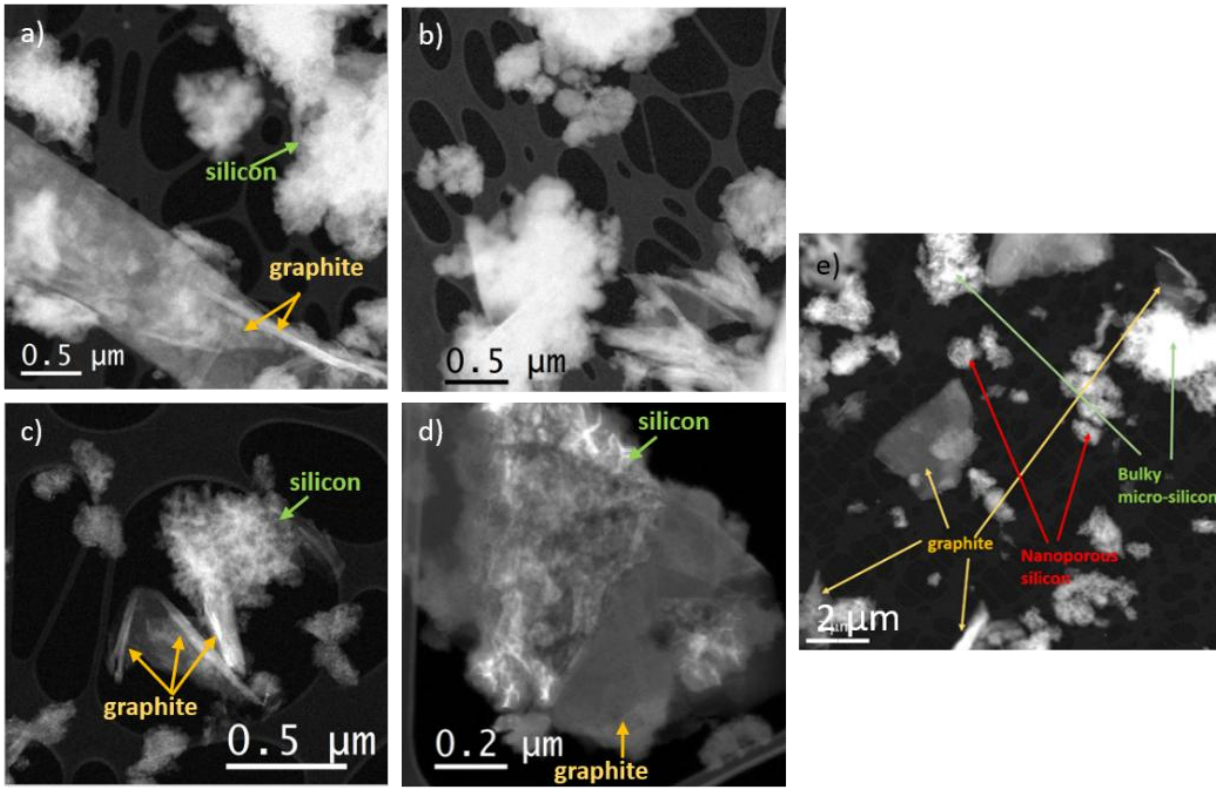


**Figure S12.** Typical STEM-HAADF image obtained on silicon electrodes after 30 cycles, initially neutralized at a-b) pH 2.5, the graphite slabs can be clearly identified as straight pieces either lying flat or edge on; c-d) pH 4. In Figure c) the graphite flakes can be clearly identified around the middle of the image, seen partly edge-on. A piece of graphite is also seen embedded in the silicon de-structured aggregate (above middle of image) in Figure d). e) pH 6, all white flakes on top or around are silicon. Morphologies of graphite and silicon (nanoporous and bulky micro) can be clearly seen (noted with arrows).

**Getting quantitative phase maps from STEM-VEELS.** – Briefly described in the 5.6 section of the experimental part of the manuscript, we here give further details on the process for obtaining representative quantification of phases thanks to STEM-VEELS. This method is based on the work of M. Boniface's PhD thesis (Ref 70). Once the percentages of phases are obtained by MLLS fit of each pixel of the map, each % is multiplied by the local value of $t/\lambda$ (proportional to the local thickness, t). $\lambda$ is the inelastic mean free path of the electrons at 300 kV (in the order of ~100 nm). The $t/\lambda$ value is obtained by the Fourier-Log method applied to the VEELS spectrum at each pixel. In doing so, the values for each phase obtained

in each pixel is proportional to the volume fraction of the phase. Intensities of all pixels for each phase are summed up in the map. The process is performed for each map (dozens of calculations). Since the experimental parameters are kept constant for all samples and maps (electron beam intensity, pixel size, …), it is admissible to compare results from one sample to another and also to sum-up all map results acquired on a same sample. In doing so, the statistics can be vastly improved and volume percentages can get closer to those present within the whole electrode.

**$Li_xSi$ alloy composition after 100 cycles. -** Energies of the plasmon peaks in all VEELS-SI obtained on electrodes cycled 100 times were much lower than the 16.5-16.7 eV value found for previous cycles. The value is close to 14.4 eV but can vary within the fluffy silicon. In order to illustrate such results, we present in **Figure S13** a map of the $E_p$ position, when fitted with a Drude model (as in **Figure S9**). A trace along this map illustrates the variability of this value shown in **Figure S13b**, which here varies between 14.4 eV and 15.4 eV. Lithium content thus varies from x=1.5 to x=1 (for a formula $Li_xSi$) exploiting formulae from Boniface's PhD thesis.[35]

Since large regions of the same compositions could be evidenced for the alloy (for Ep=14.4 eV), it was possible to extract a reference spectrum from a chosen VEELS-SI. The reference spectrum was consequently used in all MLLS fits for 100 cycles electrodes. An example of the fit high quality is given in **Figure S14**.

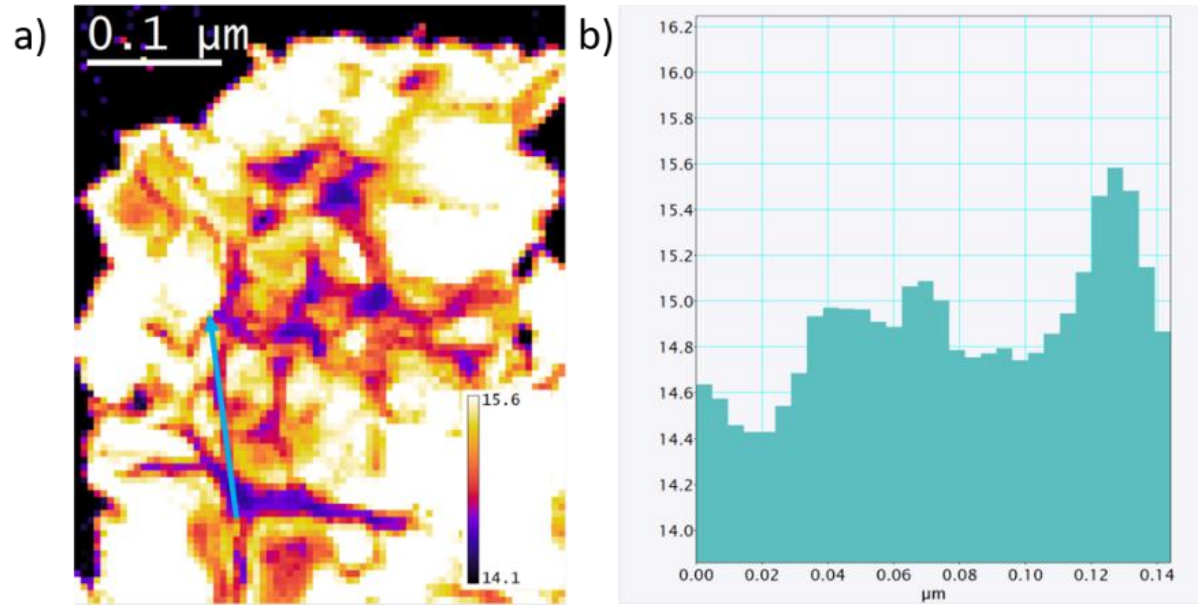


**Figure S13.** a) Map of the plasmon energy (Ep) using a Drude model. Roughly the same results were obtained with the determination of $E_{max}$ so that variation cannot be assigned to changes on the FWHM of the peak model. b) A trace of the Ep values (corresponding to the blue arrow in a). Filaments correspond generally to higher value of Ep, hence lower Li content in the $Li_xSi$ alloy.

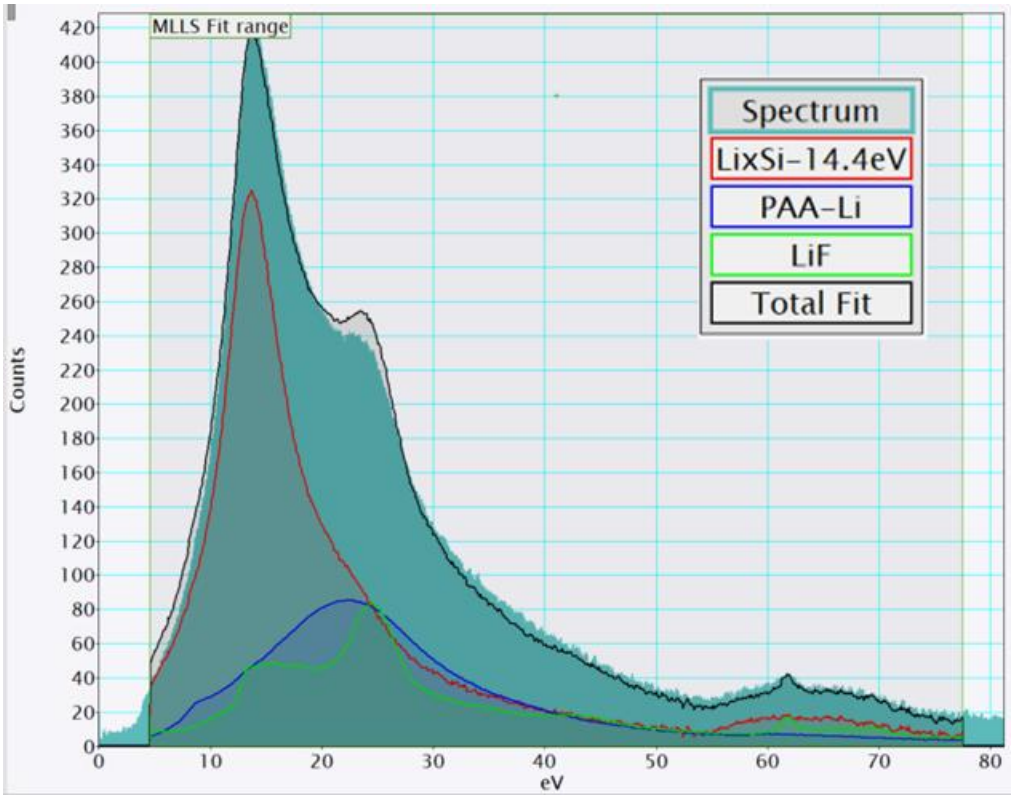


**Figure S14.** Example of decomposition of a VEELS spectrum (filled turquoise area) leading to the phase maps in the case of electrodes cycled 100 times. Reference spectra for LiF (green), PAA-Li (blue) and the alloy $Li_xSi$ with $E_p$=14.4 eV (red) were used. The resulting spectrum in black fits well the experimental spectrum of the selected region.

III - MAS NMR analysis.

The $^{7}$Li MAS NMR asymmetric peaks obtained for cycled electrodes indicate that at least two different Li local environments are present in the SEI. Based on our previous study of SEI species forming at the surface of Si/Gr particles, the sharp component at approx. -2 ppm is linked to lithiated species deposited on the silicon surface whereas the broad component at approx. -15 ppm is linked to lithiated species deposited on the graphite surface as shown for silicon (Si) and silicon/graphite (Si/Gr) reference samples mixed with LiF (**Figure S15a**). For the $^{19}$F NMR, a similar phenomenon is noticed as the presence of graphite seems also to influence the $^{19}$F NMR signal, broadening it and shifting it towards more negative NMR shifts (**Figure S15b**). Unlike $^{7}$Li NMR spectra, the strong overlap of the two relatively broad resonances attributed to fluorinated species at the surface of silicon or at the surface of graphite, as well as their sidebands, makes it impossible to clearly differentiate their respective contributions.

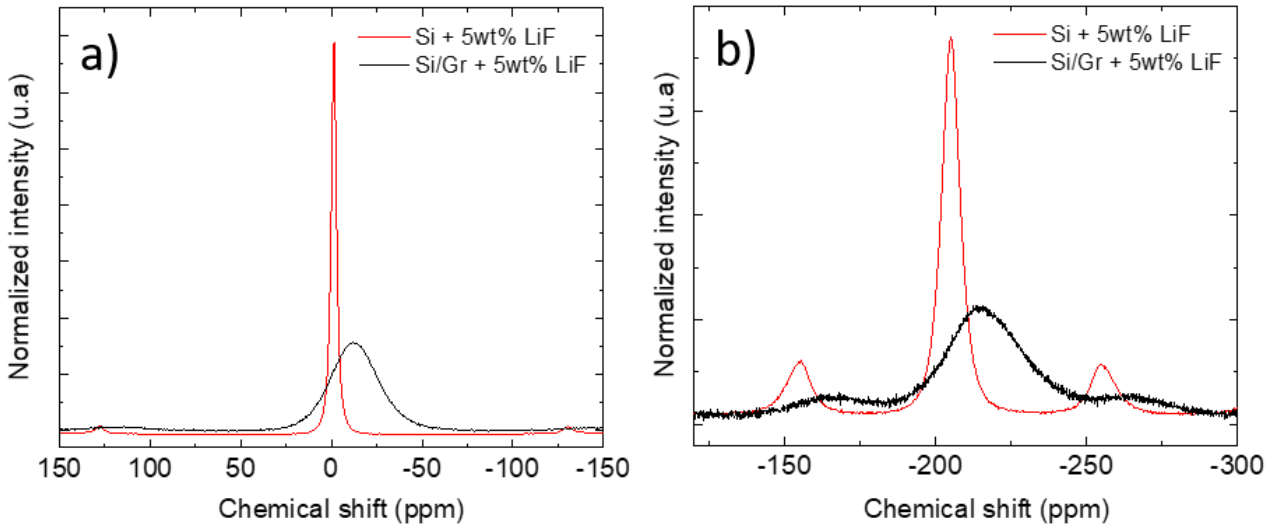


**Figure S15.** MAS-NMR characterizations of reference materials of Si + 5wt% LiF and Si/Gr + 5 wt% LiF, for a) $^{7}$Li analysis and b) $^{19}$F analysis.

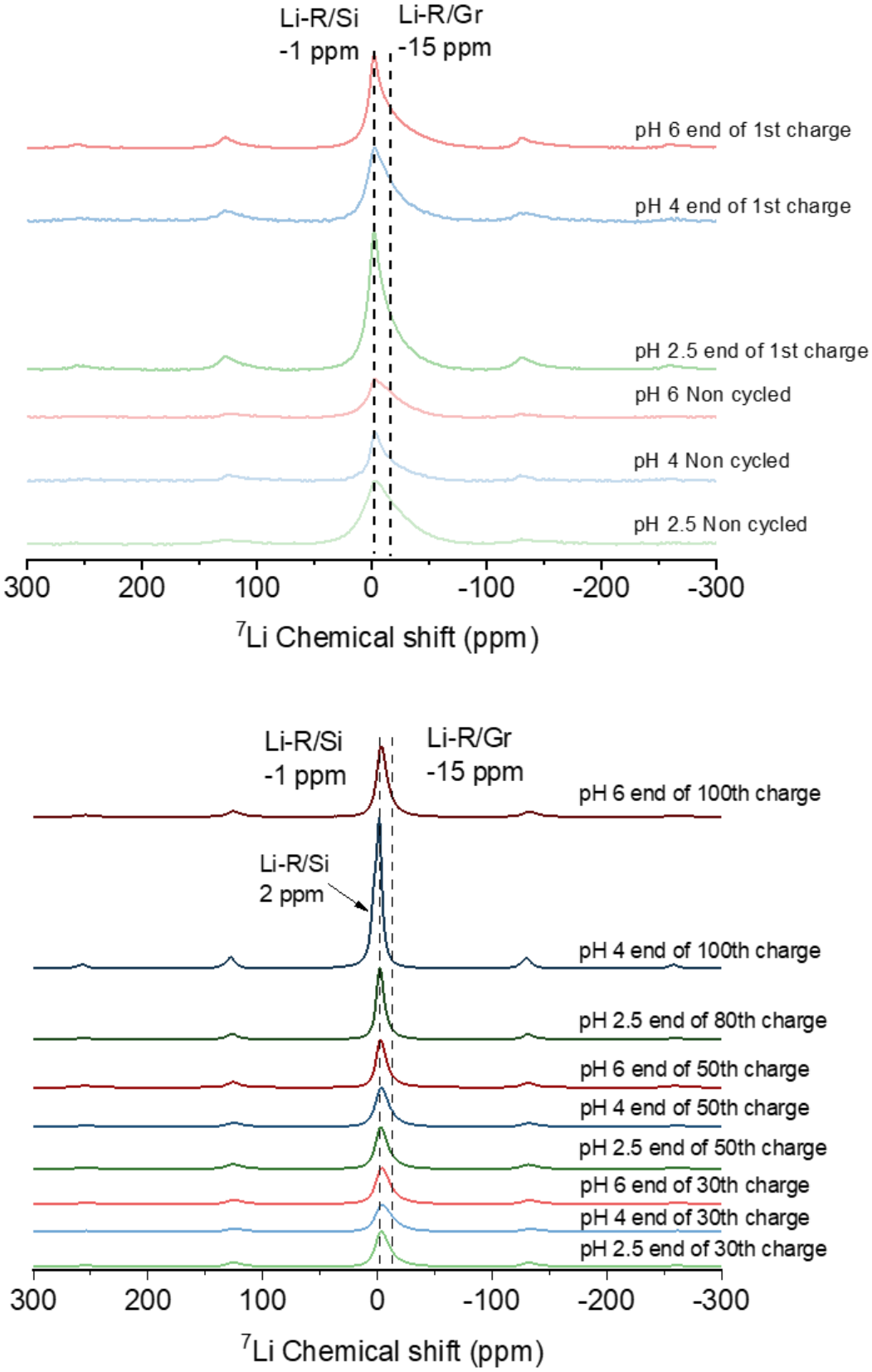


**Figure S16a.** Normalized $^{7}$Li MAS NMR spectra for electrode prepared at pH 2.5, 4 and 6, before cycling (with electrolyte wetting) and at the end of 1$^{st}$, 30$^{th}$, 50$^{th}$ and 80$^{th}$ (for pH 2.5) or 100$^{th}$ charge.

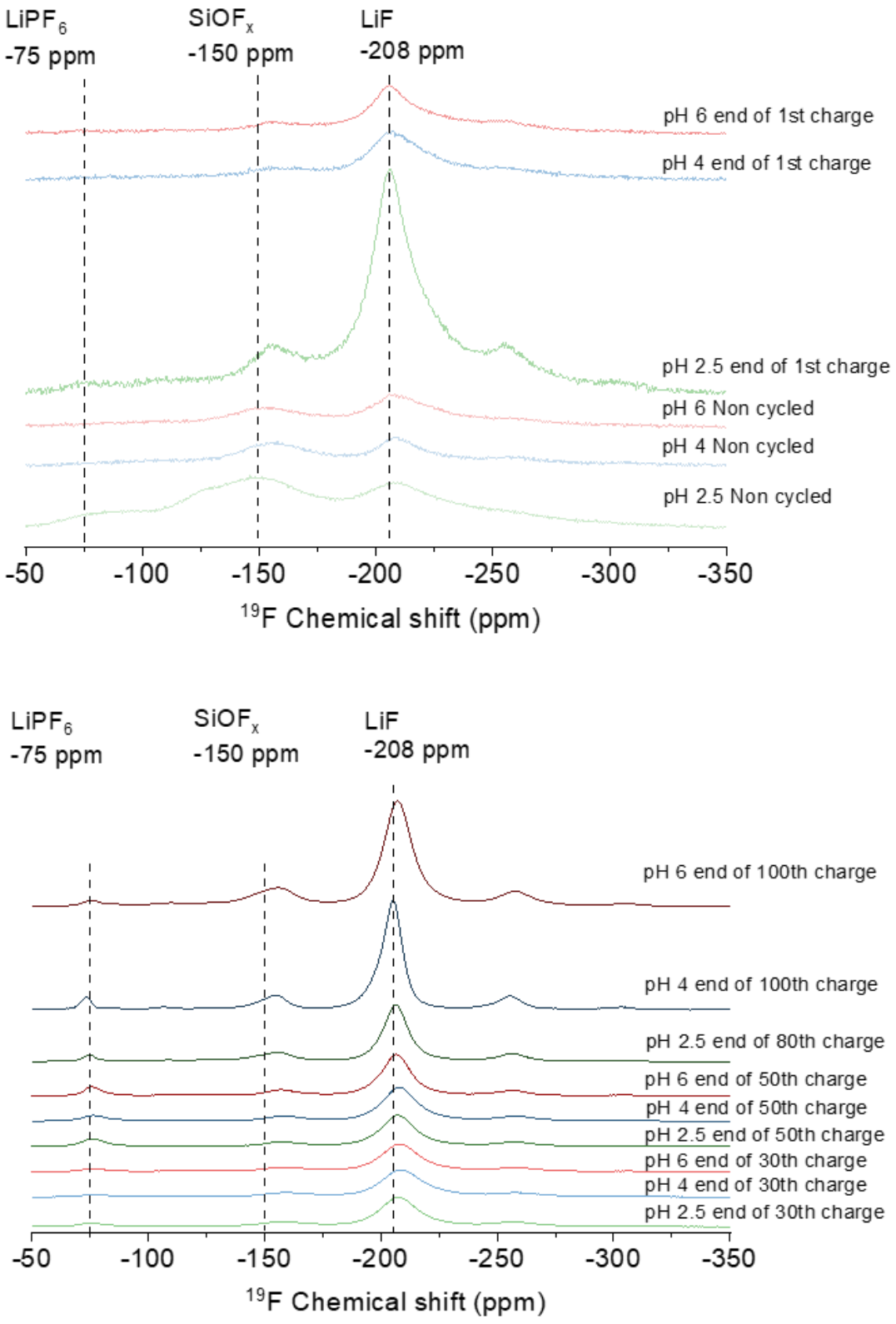


**Figure S16b.** Normalized $^{19}$F MAS NMR spectra for the electrode prepared at pH 2.5, 4, and 6, before cycling (with electrolyte wetting) and at the end of 1$^{st}$, 30$^{th}$, 50$^{th}$, and 80$^{th}$ (for pH 2.5) or 100$^{th}$ charge.

IV - SEM imaging on the electrode surface.

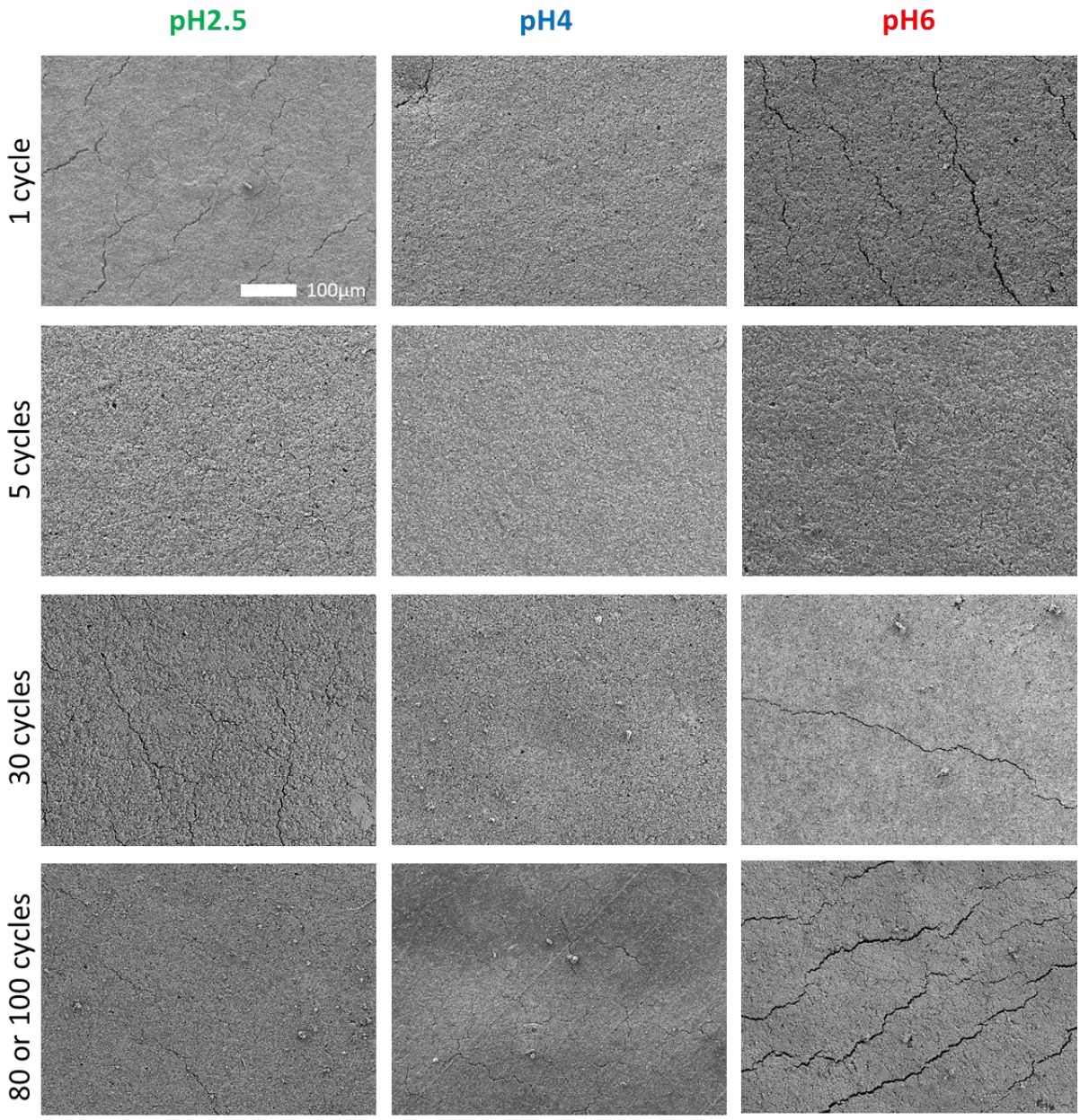


**Figure S17.** Comparison of morphological behavior of electrode surface after 1, 5, 30 and 80 (pH 2.5) or 100 cycles (pH 4 and 6).

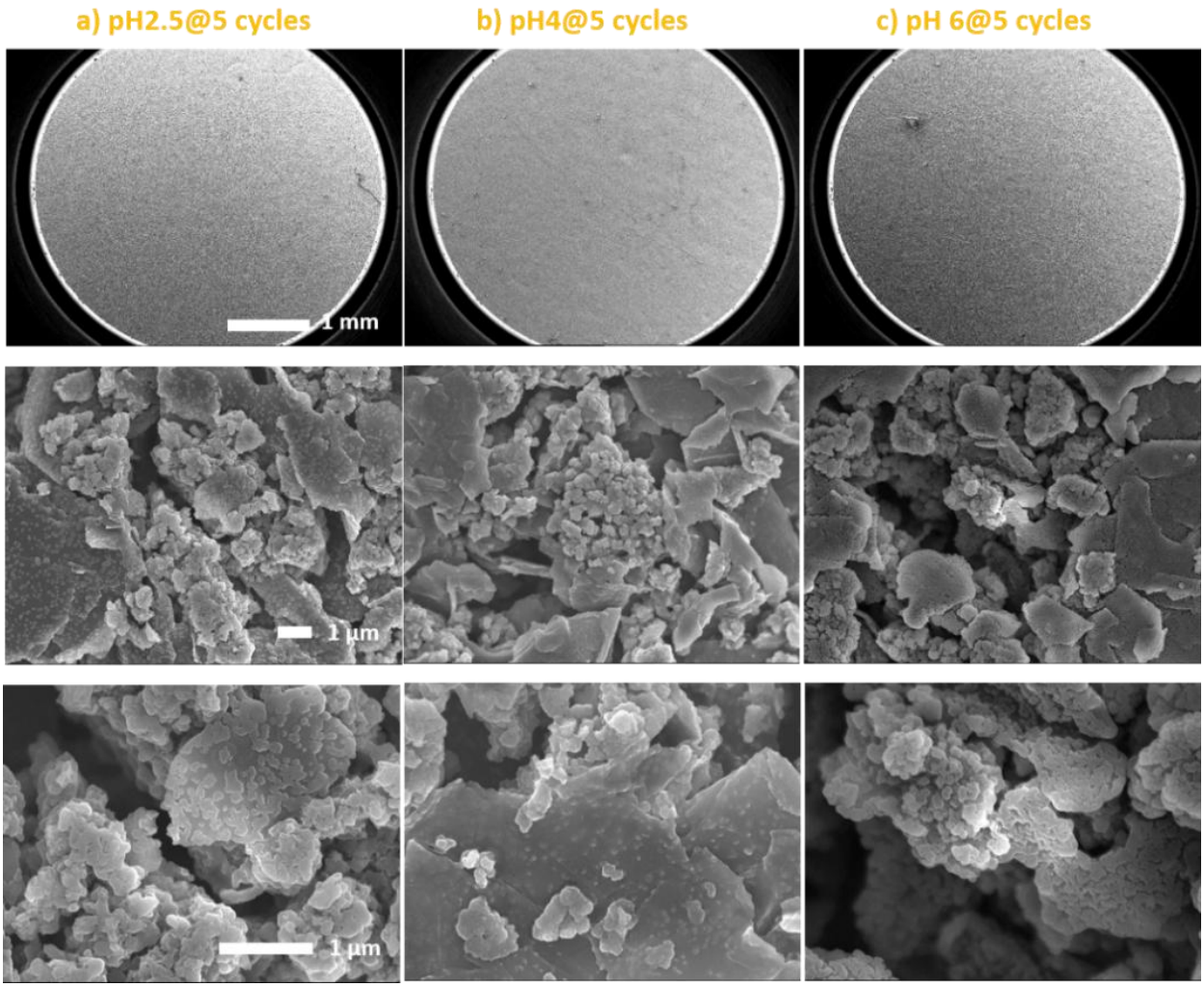
a) pH2.5@5 cycles
b) pH4@5 cycles
c) pH 6@5 cycles
1 mm
1 µm
1 µm

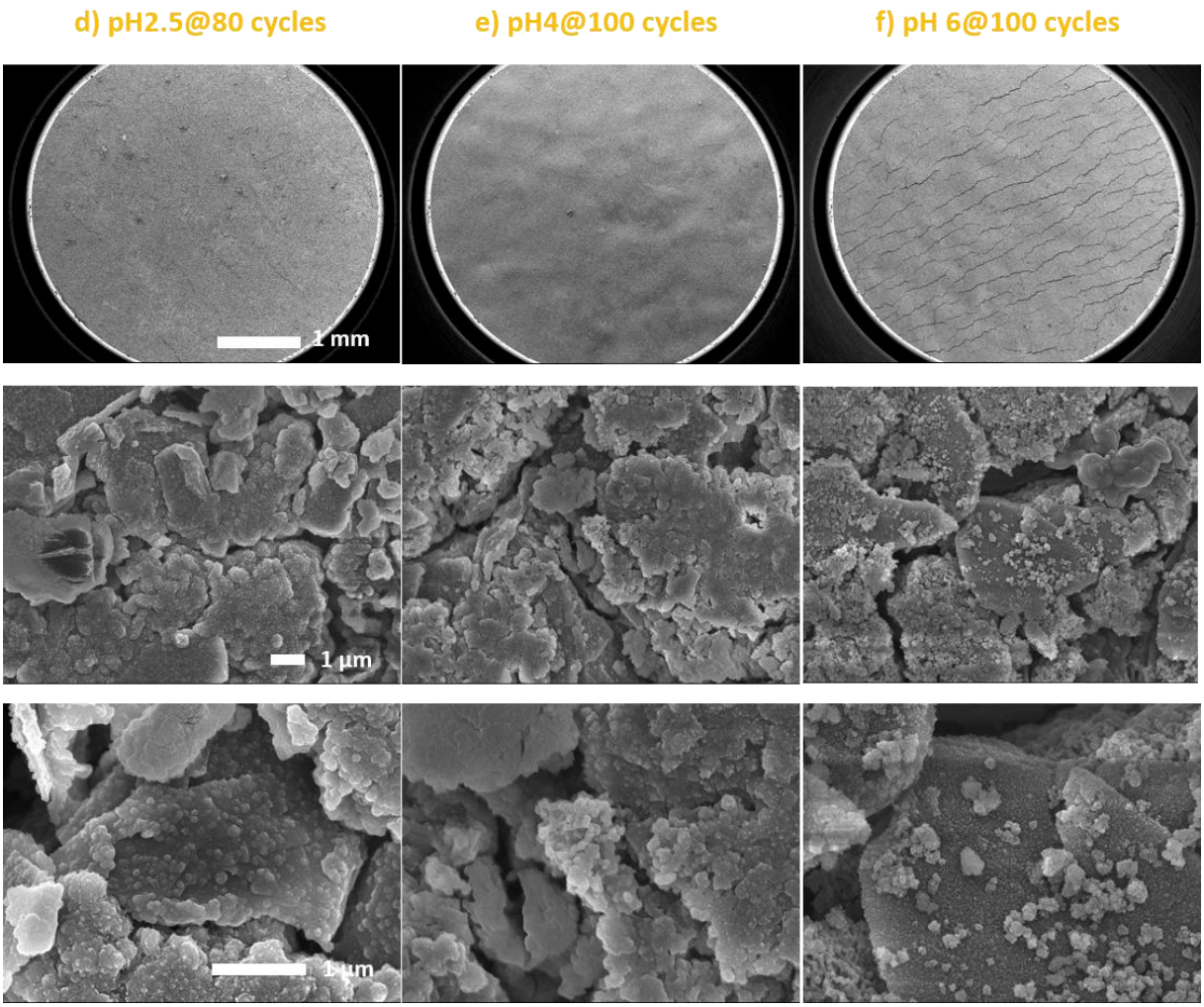


**Figure S18.** Comparison of morphological behavior of the electrode surface after 5 and 80 (for pH 2.5) or 100 cycles a,d) at pH 2.5; b,e) at pH 4; c,f) at pH 6 at other magnifications.

V - "Capacity jump" behavior with Swagelok cell.

Cycling with Swagelok cells were performed under the same conditions (electrodes, loadings, electrolytes, current rate) as with coin cell. As can be seen (**Figure 1a** and **Figure S19a-c**), Swagelok cells and coin cells display different behaviors, especially at pH 4 and pH 2.5, and to a much lesser extent at pH 6. Unlike the decrease continuous capacity observed in the coin cell configuration, at pH 4 a sharp decrease in capacity is observed, followed by a sudden recovery of capacity, in a cyclic way (**Figure S19b**). These jumps in capacity gradually subside and finally disappear after 70 cycles. We assume that the cause of this phenomenon is

the difference in internal pressure inside the cells.[47] In the case of Swagelok cells, the low internal pressure, due to the low stiffness spring, does not constrain the expansion of the electrode, making possible its delamination from the current collector. We have indeed observed this phenomenon by various measurements carried out with electrochemical cells in which a very low pressure is applied to the electrode (operando optical microscopy, electrochemical dilatometry, and in situ X-ray tomography).[18,46] This delamination of pieces of electrode results in loss of capacity due to loss of direct electrical contact with the current collector. The increase in capacity loss with the number of cycles reflects the progress of delamination of the electrode film. Recovery of the lost capacity results from reestablishing contact between this piece of electrode and the current collector, possibly following its fracturing (**Figure S19d**). This overall process then starts again until the next capacity jump.[50] Notably, this phenomenon is not observed in the case of the electrode prepared at pH 6. However, this one is more fragile, as evidenced by its low resistance to the scratch test,[27] and its cracking observed with the SEM after 1 cycle in coin cell (Figure 4). This weak cohesion, which causes the electrode to crumble, likely explains the lack of capacity jumps in Swagelok. Correspondingly, the observation of this phenomenon for the electrode prepared at pH 4 relates to the greater cohesion of the electrode film, which causes it to blister in response to the expansion of the silicon (Figure S16d). In the case of coin cells, the strongest internal pressure makes it possible to press the electrodes against the current collector and thus not to lose this electrical contact. In the case of the electrode prepared at pH 2.5, the behavior is intermediate to that of the other two electrodes (presence of moderate capacity jumps). This is due to either stronger adhesion to the current collector or greater rigidity of the electrode film,[27] promoting fracturing of the film in response to its expansion.

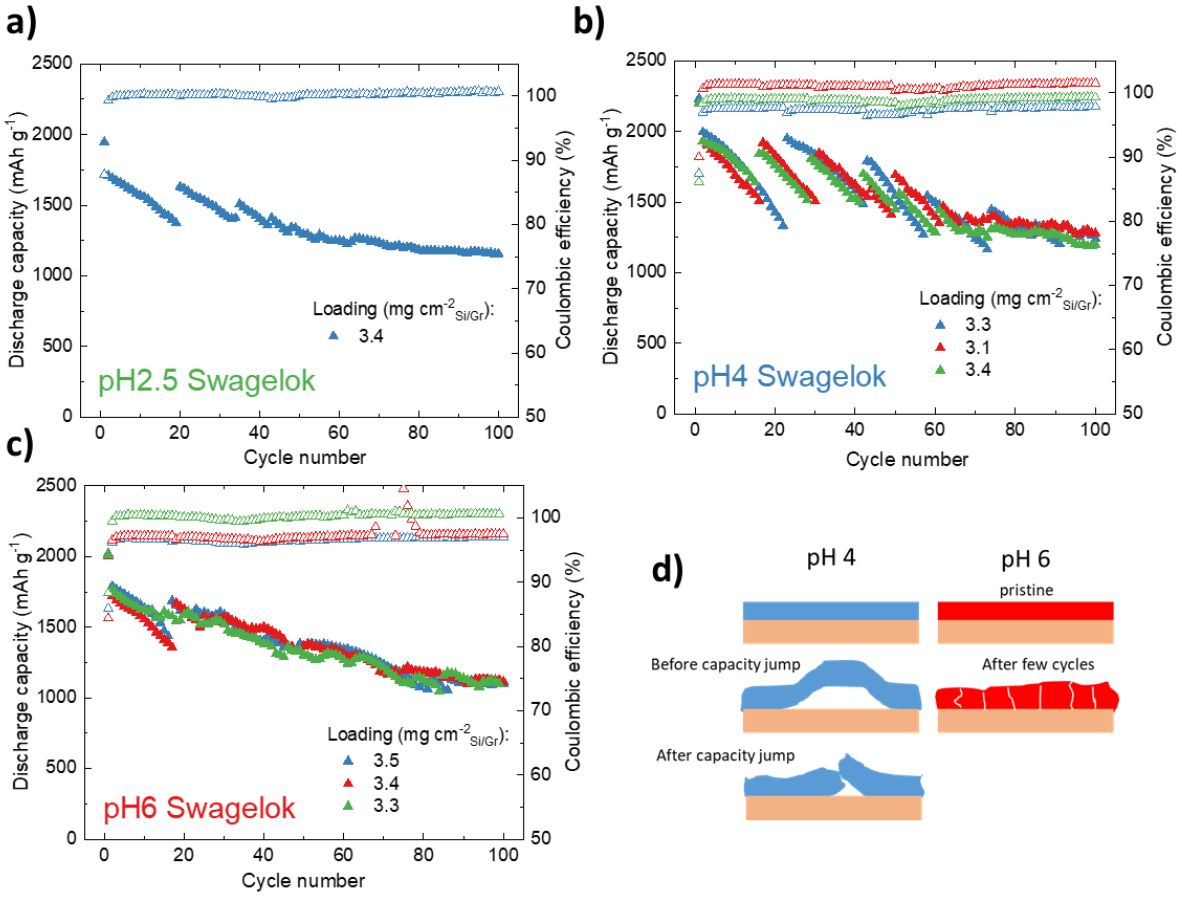


**Figure S19.** Half-cell electrochemical cycling in Swagelok cells of Si/Gr electrode prepared at pH a) 2.5, b) 4 and c) 6. d) Schematic representation of the mechanical behavior of the electrode film to the volume expansion of silicon according to the cohesion of the electrode (high at pH 4 and low at pH 6).

## VI - NMC electrode cycling .

A more thorough study of the NMC 532 electrodes used here is presented elsewhere.[72]

**Table S1** : Compositions and characteristics of NMC electrode used in full-cell tests. CB: Carbon Black; CNT: Carbon NanoTubes.

**Compositions (wt%):**

| NMC 532 | CB | PVdF | CNT |
|---|---|---|---|
| 95.9 | 1.1 | 1.8 | 1.2 |

**Characteristics:**

| Density (g $cm^{-3}$) | Porosity (%) | Thickness (µm) |
|---|---|---|
| 3.4 | 23.6 | 76.6 |

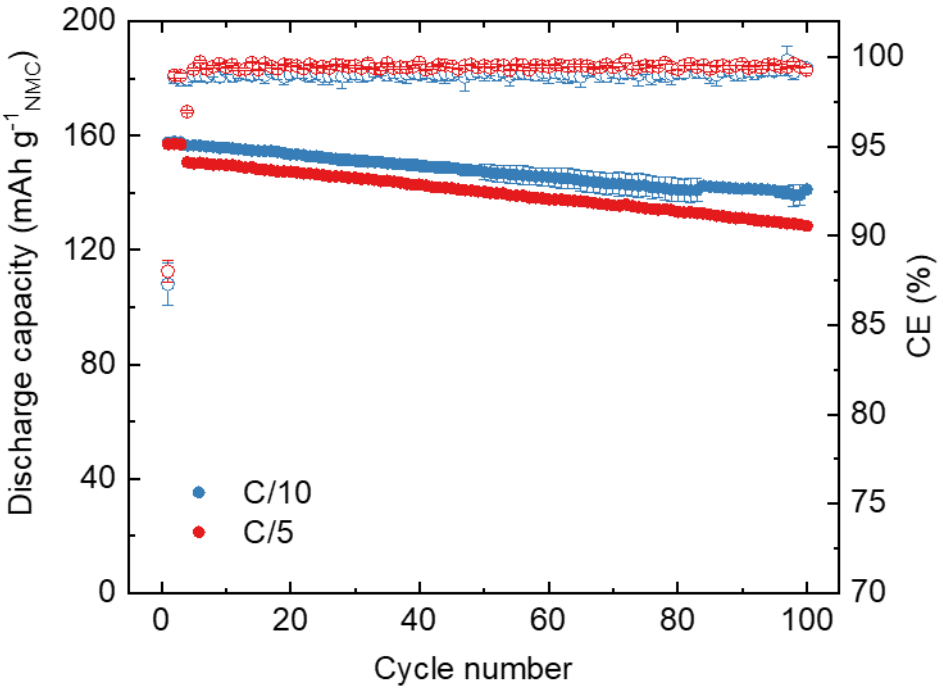


**Figure S20.** Half-cell cycling of the NMC electrode at C-rate of C/10 and C/5 in an FEC-rich and EC-free electrolyte (1M $LiPF_6$ in DMC/FEC 70/30 v/v). Voltage scan was defined between 2.5-4.3 V *vs.* $Li^+/Li$.

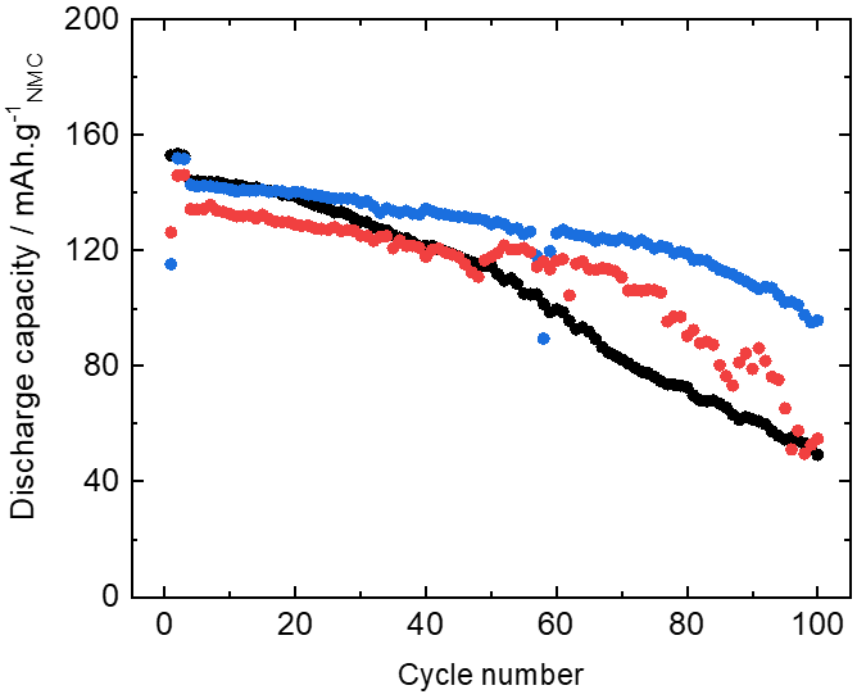


**Figure S21.** Half-cell cycling of NMC electrode at C-rate of C/5 in a classical LP30 electrolyte (1M $LiPF_6$ in EC/DMC 50/50 v/v).

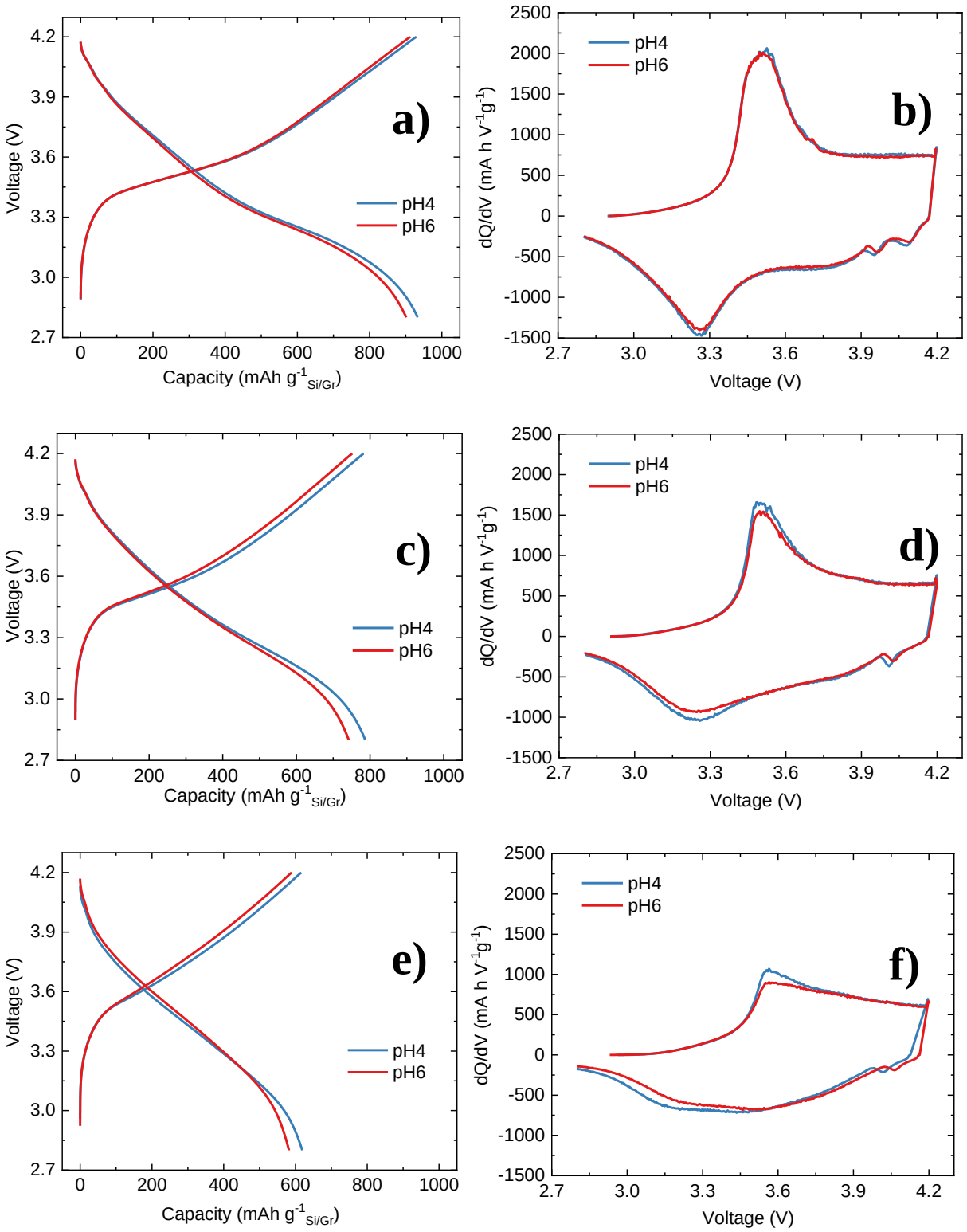


**Figure S22.** Comparison of voltage profiles and incremental capacity curves of pH 4, and 6 electrodes for the: a-b) 1st, c-d) 50th and e-f) 100th cycles in full cells.